

RESEARCH ARTICLE

10.1029/2018JD029164

Key Points:

- Wind and temperature revealed in the first year-round radiosonde at Jang Bogo Station (a new Antarctic station since 2014) are investigated
- Characteristics, energy, and momentum flux of inertia-gravity waves revealed in the radiosonde data at Jang Bogo Station are examined

Supporting Information:

- Supporting Information S1

Correspondence to:

H.-Y. Chun,  
chunhy@yonsei.ac.kr

Citation:

Yoo, J.-H., Choi, T., Chun, H.-Y., Kim, Y.-H., Song, I.-S., & Song, B.-G. (2018). Inertia-gravity waves revealed in radiosonde data at Jang Bogo Station, Antarctica (74°37'S, 164°13'E): 1. Characteristics, energy, and momentum flux. *Journal of Geophysical Research: Atmospheres*, 123, 13,305–13,331. <https://doi.org/10.1029/2018JD029164>

Received 12 JUN 2018

Accepted 2 NOV 2018

Accepted article online 8 NOV 2018

Published online 12 DEC 2018

Author Contributions:

**Data curation:** T. Choi

**Formal analysis:** H.-Y. Chun, Y.-H. Kim, I.-S. Song

**Investigation:** J.-H. Yoo

**Methodology:** Y.-H. Kim, I.-S. Song, B.-G. Song

**Resources:** T. Choi

**Supervision:** H.-Y. Chun







**Validation:** J.-H. Yoo

**Visualization:** J.-H. Yoo, B.-G. Song

**Writing - original draft:** J.-H. Yoo, H.-Y. Chun

**Writing - review & editing:** T. Choi, H.-Y. Chun, Y.-H. Kim, I.-S. Song, B.-G. Song

# Inertia-Gravity Waves Revealed in Radiosonde Data at Jang Bogo Station, Antarctica (74°37'S, 164°13'E): 1. Characteristics, Energy, and Momentum Flux

J.-H. Yoo<sup>1</sup> , T. Choi<sup>2</sup> , H.-Y. Chun<sup>1</sup> , Y.-H. Kim<sup>3</sup> , I.-S. Song<sup>2</sup> , and B.-G. Song<sup>1</sup> 

<sup>1</sup>Department of Atmospheric Sciences, Yonsei University, Seoul, South Korea, <sup>2</sup>Division of Polar Climate Research, Korea Polar Research Institute, Incheon, South Korea, <sup>3</sup>Institut für Atmosphäre und Umwelt, Goethe Universität Frankfurt, Frankfurt, Germany

**Abstract** Characteristics of inertia-gravity waves (IGWs) at high latitude in Antarctica are investigated using radiosondes launched daily at Jang Bogo Station (74°37'S, 164°13'E), a new Antarctic station that has been operating since 2014, in the troposphere ( $z = 2\text{--}7$  km) and lower stratosphere ( $z = 15\text{--}22$  km) for 25 months (December 2014 to December 2016). The vertical propagation of IGWs exhibits strong seasonal variations in the stratosphere, with an enhancement (reduction) in downward (upward)-propagating IGWs from May to mid-October. In the troposphere, both upward- and downward-propagating IGWs have similar occurrence rates without seasonal variations. The intrinsic phase velocity of IGWs mostly direct to the west (isotropic), while the ground-relative phase and group velocities are dominant in the east and southeast (northeast), respectively, in the stratosphere (troposphere). The intrinsic frequency, vertical wavelength, and horizontal wavelength of IGWs averaged in the troposphere (stratosphere) are  $3.57f$  ( $1.93f$ , where  $f$  is the Coriolis parameter), 1.48 (1.48) km, and 63.06 (221.81) km, respectively. The wave energy in the stratosphere has clear seasonal variations with large values in autumn and spring, while that in the troposphere is smaller without obvious seasonal variations. Zonal and meridional momentum fluxes averaged in the stratosphere (troposphere) are  $-0.008$  ( $-0.0018$ ) and  $-0.0005$  (0.001)  $\text{m}^2/\text{s}^2$ , respectively. The momentum flux of downward-propagating IGWs in the stratosphere is mostly positive in both zonal and meridional directions, whereas the directional preference is not obvious in the troposphere. In Part 2, sources of the observed IGWs in the troposphere and stratosphere will be examined.

## 1. Introduction

Vertically propagating atmospheric gravity waves (GWs) transfer their energy and momentum to the middle atmosphere when they are dissipated (Lindzen, 1981). The momentum forcing by GWs plays a major role in driving a one-cell meridional gyre in the mesosphere (Andrews et al., 1987; Fritts & Alexander, 2003; Garcia & Boville, 1994), and they contribute to the Brewer-Dobson circulation in the stratosphere along with planetary waves (Butchart et al., 2010; Chun et al., 2011; Randel et al., 2008). GWs are not fully resolved from the current resolutions of general circulation models (GCMs), even in recent high-resolution GCMs, with a horizontal grid spacing of  $\sim 25$  km (Preusse et al., 2014); thus, their effects should be parameterized in GCMs (Kim et al., 2003). Although there have been significant efforts to improve GW drag (GWD) parameterization during the past three decades, uncertainties still exist in GWD parameterization schemes used in current GCMs (Geller et al., 2013). Particularly, in the polar stratosphere of the Southern Hemisphere (SH), the magnitude of the GW momentum flux observed from satellites is the largest among those at all latitudes, and the discrepancies in the GW momentum flux between the observed and parameterized from GCMs are most prominent (Geller et al., 2013). In addition, an excessive polar night jet and associated cold bias in the SH polar stratosphere, which has been a long-lasting problem in most GCMs, are likely due to the missing GWD in this area either by mountain waves in the downstream that are not fully represented from a columnar GWD scheme used mostly in current GCMs (Garcia et al., 2017; McLandress et al., 2012) or by convective GWs that are generated from SH storm tracks in winter that propagate poleward (Choi & Chun, 2013). To advance our understanding on GWs in the SH polar region and improve GWD parameterization schemes in GCMs, more observational and numerical modeling studies on GWs over Antarctica are required.

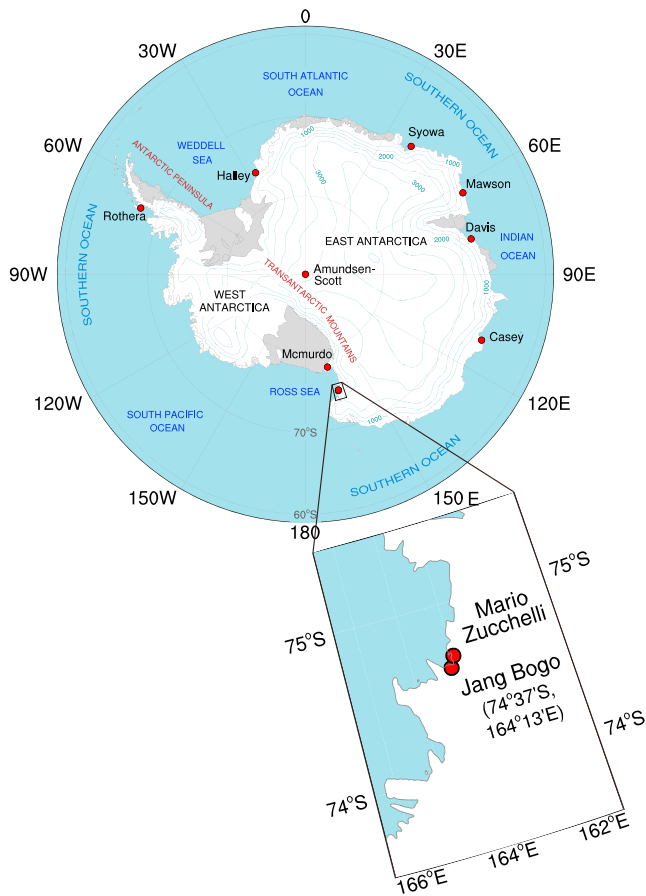


**Figure 1.** Map of Antarctica. Meteorological stations conducting radiosonde observations in Antarctica are indicated by red circles. The zoomed map shows the geographical locations of Jang Bogo Station and Mario Zucchelli Station.

Various observational instruments have been used to investigate GWs over Antarctica, such as lidar (Innis et al., 2008; Yamashita et al., 2009), radar (Alexander et al., 2017; Fritts et al., 2012; Love & Murphy, 2016), superpressure balloons (Hertzog et al., 2007, 2008), radiosondes (Innis et al., 2004; Moffat-Griffin et al., 2011; Murphy et al., 2014; Pfenninger et al., 1999; Yoshiki et al., 2004; Yoshiki & Sato, 2000), all-sky airglow imaging (Matsuda et al., 2017; Rourke et al., 2017), and satellites (Alexander et al., 2010; Jiang et al., 2002; Wu & Jiang, 2002). Among these, radiosondes have been actively employed for GW studies, as they can detect GWs at a wide range of vertical wavelengths for a long time period over various geographical locations. From previous studies on the climatology of GWs in the Antarctic stratosphere using radiosonde data, some common features have been found: (i) clear seasonal variations in GW activities with a maximum in spring and (ii) an increase in the number of downward-propagating GWs from late autumn to early spring (Moffat-Griffin et al., 2011; Murphy et al., 2014; Pfenninger et al., 1999; Yoshiki et al., 2004; Yoshiki & Sato, 2000). Yoshiki and Sato (2000) identified the seasonal variations in wave energy with a maximum in spring over Antarctica, based on radiosonde data obtained from 33 stations in the polar regions for 10 years (1987–1996). They found that topography was not a main source of GWs in Antarctica, unlike in Arctic. Yoshiki et al. (2004) investigated the temporal and altitudinal variations in GW energy using radiosonde data obtained from Syowa (69°0'S, 39°3'E) Station for 2 years (1997–1999). In an altitudinal region of 15–25 km, GW activity has a maximum in spring, which is associated with a polar vortex approaching Syowa Station, while in the altitudinal region of 13–15 km, the GW energy increases more frequently when tropospheric disturbances pass over the station without evident seasonal variations. On the other hand, Moffat-Griffin et al. (2011) found that orographically induced GWs contribute to the GWs observed in the stratosphere above the Antarctic Peninsula using 8-year (2002–2010) soundings collected from Rothera Station (67°3'S, 68°0'W), which has also been shown from the satellite observations by Ern et al. (2004). Murphy et al. (2014) examined the possible sources of downward-propagating GWs,

which increase in the lower stratosphere between early May and mid-October, using radiosonde observations from Davis Station (68°3'S, 77°5'E) for 12 years (2001–2012) by employing the wavelet method. They suggested that an imbalanced flow associated with the polar night jet in the stratosphere generates the observed GWs. Meanwhile, Pfenninger et al. (1999) investigated GW properties in the troposphere and lower stratosphere using 4-year (1993–1996) radiosonde data obtained from the South Pole and showed that there was no clear correlation between the spectral characteristics of GWs observed in the troposphere and those in the stratosphere, suggesting different sources for GWs in the troposphere and stratosphere.

In the present study, we examine the characteristics of inertia-gravity waves (IGWs) observed from radiosondes launched daily for 25 months (December 2014 to December 2016) at a new Antarctic station, Jang Bogo Station (JBS), which has been operated by the Korea Polar Research Institute since 2014. This is the first report to present radiosonde data from JBS. JBS (74°37'S, 164°13'E) is located in the mainland of Antarctica, at Terra Nova Bay in northern Victoria Land (Figure 1). The surface winds at JBS are strongly influenced by katabatic winds flowing from the high-elevation Transantarctic Mountains, which divide West and East Antarctica, throughout the year. Due to the influence of the Transantarctic Mountains and the Ross Sea, low-pressure systems commonly appear above JBS (Wang et al., 2017). The Transantarctic Mountains, which are located at the windward side of JBS, can be a potential source of GWs in this region. In addition, tropospheric disturbances induced by low-pressure systems above the JBS can generate GWs. The polar night jet in the stratosphere, which is located at 50–70°S, is likely another important source that generates GWs, especially for downward-propagating GWs in the troposphere and lower stratosphere. Due to the extremely cold and dry atmosphere in this region, convection or surface fronts can rarely develop near JBS. However, it should

**Table 1**  
*Information on the Radiosonde Data Observed at Jang Bogo Station, Antarctica (74°37'S, 164°13'E) Used in This Study*

Model	Variables	Vaisala GPS radiosonde (RS92G)	
Observation		Resolution	Accuracy
	Temperature (°C)	0.1	0.5
	Pressure (hPa)	0.1	1 (1,080–100) 0.6 (100–3)
	Wind direction (deg)	1	2
	Wind speed (m/s)	0.1	0.15
Period		14 December 2014 to 20 December 2016 (25 months)	
Launch frequency		Once a day (between 23 and 01 UTC)	
Resolution	Temporal (s)	2	
	Vertical (m)	~10	

*Note.* GPS = global positioning system.

be noted that IGWs can propagate long horizontal distances from their source regions; therefore, the sources of GWs observed in the stratosphere are not necessarily near the observation stations, which has also been shown in Chun et al. (2007), Ki and Chun (2010), and Ki and Chun (2011). To examine the potential sources of GWs observed at JBS, it is necessary to calculate the trajectory of waves using a three-dimensional ray-tracing model for IGWs, which will be performed in Part 2.

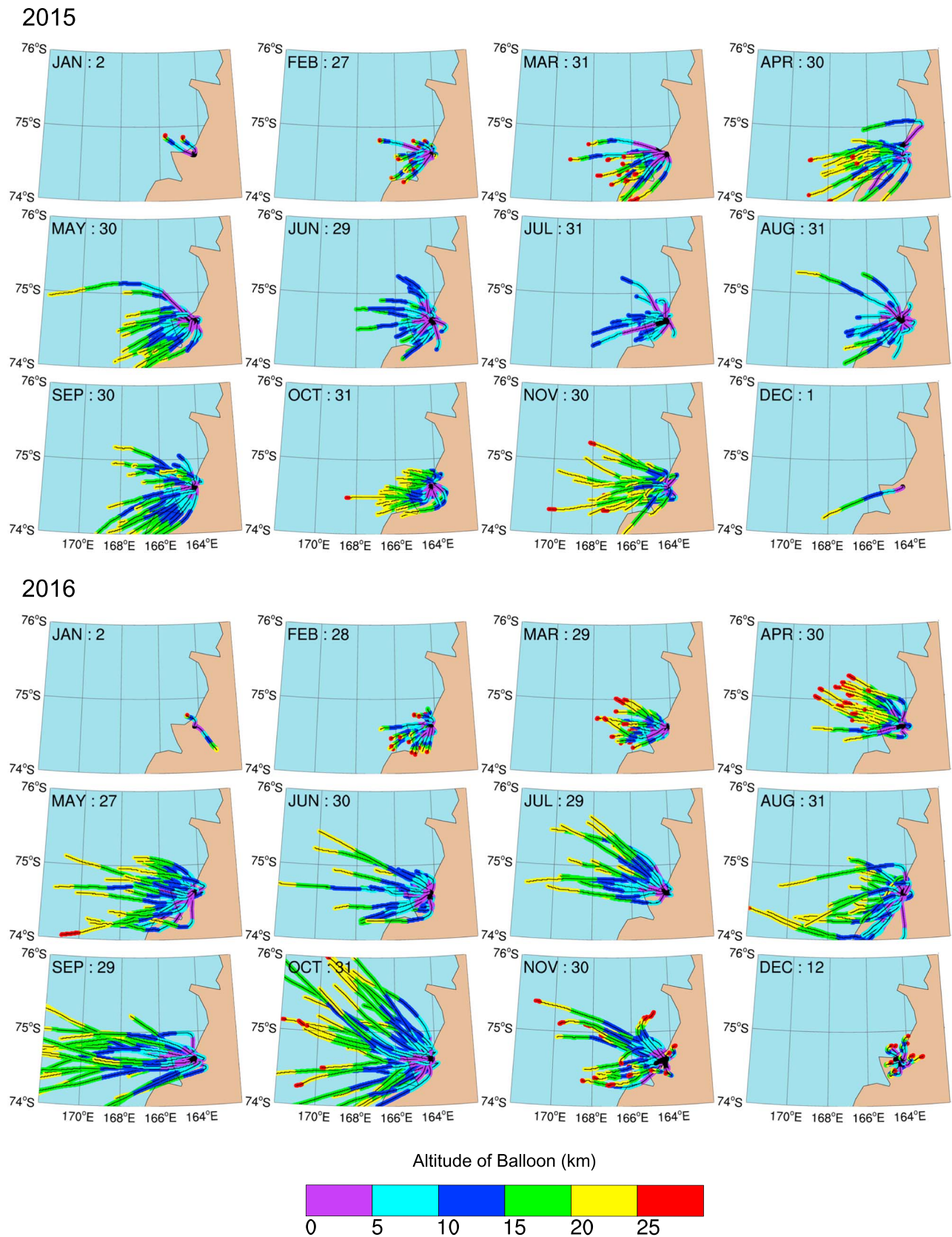
Over the Antarctic continent, where in situ measurements of meteorological variables are much more difficult and expensive compared with those in areas at the midlatitudes, radiosonde observations at JBS for longer than 2 years are invaluable resources that enable us to investigate the characteristics, energy, and momentum of GWs. In the following section, details of radiosonde data are given, and the wind and temperature structures revealed in the observations are compared with those from the reanalyses. In section 3, the characteristics of IGWs, wave energy, and momentum flux are shown. In section 4, the characteristics of IGWs above JBS are compared with those at other Antarctic stations. Finally, summary and concluding remarks are given in section 5.

## 2. Data and Analysis Methods

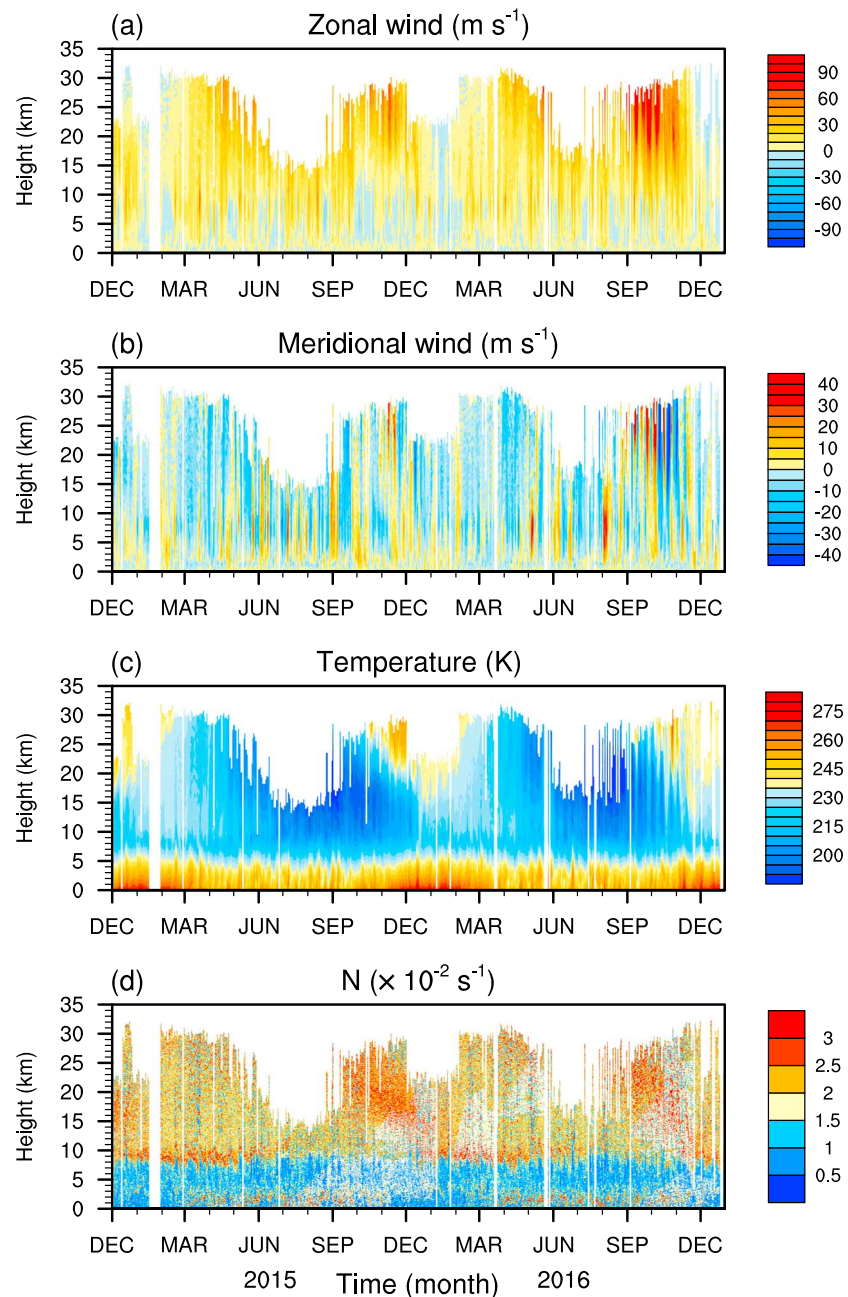
In this study, radiosonde data obtained at JBS from December 2014 to December 2016 are used to examine the characteristics of IGWs. Figure 1 illustrates the locations of JBS and other research stations that have performed GW research previously using radiosonde observations (denoted by red circles). The results of the GW research at some of these stations and a comparison with the current results will be discussed in section 4. Observations were obtained once a day between 2300 and 0100 UTC using the Vaisala RS92G radiosonde. The temperature, pressure, and relative humidity are measured, and the wind speed and direction are calculated using a global positioning system (GPS) every 2 seconds. With an ascending velocity of approximately 5–6 m/s, approximate 10-m vertical resolution data are obtained. The details, including the resolution and accuracy of each observed variable, are shown in Table 1.

Figure 2 describes the trajectories of the balloons each month. The number written in the upper-left corner of each panel denotes the number of soundings launched each month. Because there is no GPS information on the location of the balloons launched in December 2014, the trajectories during that period are not shown in this figure. Most of the balloons drift eastward via prevailing westerlies during their ascent. Corresponding to the background wind (especially the polar night jet), the typical drift distance ranges from approximately 30 km (January) to 306 km (September). The maximum height of the observations is approximately 30–35 km during austral summer, while it is reduced to 20 km during austral winter (Figure 3), as the elasticity of the balloon decreases significantly in winter due to the extremely cold temperature in the lower stratosphere.

The number of balloons in December and January is much smaller compared to that in other months; this is because in that period, radiosonde observations are carried out at Mario Zucchelli Station (MZS; 74°4'S, 164°0'E) instead of at JBS, which is the nearest Italian station located southwest of JBS (approximately 10 km), as shown in a zoomed map in Figure 1. MZS has been carrying out radiosonde observations twice



**Figure 2.** Trajectories of the soundings each month from 2015 to 2016. The trajectories are plotted in different colors depending on the altitude of the balloons.



**Figure 3.** Time-height cross sections of the (a) zonal wind ( $U$ ), (b) meridional wind ( $V$ ), (c) temperature ( $T$ ), and (d) Brunt-Väisälä frequency ( $N$ ) at Jang Bogo Station.

a day during the summer period (November to January) since 1998. When we compare the wind and temperature observations obtained from the 61 soundings launched on the same day at JBS and MZS, two observations are consistent enough. Examples of the zonal wind, meridional wind, and temperature profiles obtained at JBS and MZS are shown in Figure S1, and a detailed comparison of the results between the two stations can be found in Text S1. Therefore, we include the MZS radiosonde observations in the present study for dates when no observations were carried out at JBS in December and January. The original profiles are interpolated into vertically uniform spacing of 20 m using the cubic spline method. In addition, a 200-m moving average is applied to the interpolated data to remove the influence of different response times between the wind and temperature measurements (Ki & Chun, 2011). The number of profiles observed each month is shown in Table 2.

**Table 2**

*The Number of Available Radiosonde Soundings Launched Each Month, Those Passing Through the Tropospheric and Stratospheric Analysis Layers and Those Satisfying IGW Conditions in Each Layer*

Year	Month	Total profiles	Troposphere (2–7 km)		Stratosphere (15–22 km)	
			No. of available profiles	No. of profiles for IGW analysis	No. of available profiles	No. of profiles for IGW analysis
2014	December <sup>a</sup>	28	28	11	25	19
2015	January <sup>a</sup>	18	18	5	15	15
	February	27	27	14	27	27
	March	31	31	13	31	26
	April	30	30	16	28	24
	May	30	30	14	24	8
	June	29	29	15	2	1
	July	31	31	12	0	0
	August	31	31	8	5	1
	September	30	30	14	23	12
	October	31	31	15	28	21
	November	30	30	11	30	18
	December <sup>a</sup>	31	31	16	24	14
2016	January <sup>a</sup>	29	29	13	22	22
	February	29	29	17	28	26
	March	29	29	14	27	25
	April	30	30	12	30	26
	May	27	27	14	26	9
	June	30	30	16	8	2
	July	29	28	10	15	7
	August	31	31	13	22	9
	September	29	29	16	29	10
	October	31	31	14	31	16
	November	30	29	16	29	27
	December <sup>a</sup>	28	28	15	25	22
Total		729	727	334	554	387

Note. IGW = inertia-gravity wave.

<sup>a</sup>Months when data obtained from the Mario Zucchelli Station are included.

### 2.1. Wind and Temperature Observations

Given that the radiosonde data used in the present study are the first directly measured wind and temperature data at JBS, we examine the characteristics of wind, temperature, and stability revealed in the radiosonde data prior to examining the properties of GWs.

Time-height cross-sections of zonal wind ( $U$ ), meridional wind ( $V$ ), temperature ( $T$ ), and the Brunt-Väisälä frequency ( $N$ ) observed at JBS are displayed in Figure 3. In the troposphere, westerlies and easterlies are shown to alternate without a clear seasonal preference. In the stratosphere above  $z = 15$  km, westerlies are dominant from March to November, whereas weak easterlies appear between December and February. From May to October, stratospheric westerlies are intensified and developed into the polar night jet, with a maximum magnitude of approximately 122 m/s (78 m/s) in September 2016 (2015). Compared to the zonal wind, the meridional wind exhibits strong variations with time, typically ranging from  $-40$  to 50 m/s, without clear seasonal variations. However, the maximum meridional wind exceeds 78 m/s on 9 October 2016 at about  $z = 29$  km.

The near-surface temperature at JBS ranges from 240 K ( $-33$  °C) in June–September to 263 K ( $-10$  °C) in December–February, and it decreases with height and remains almost constant in the layer of  $z = 8$ –10 km. The annual temperature variations are more significant in the lower stratosphere than those in the troposphere. Significant cooling begins as the sun disappears in May, and extremely low temperatures appear during the winter months, as the atmosphere above JBS is inside the polar vortex. The lowest temperature is approximately 179 K ( $-94$  °C) at an altitudinal region of 15–20 km in August. Springtime warming occurs from the midstratosphere just after the stratospheric polar vortex begins to be weakened at the end of September, and it propagates downward and reaches the lower stratosphere after November. As a

**Table 3**  
Information on the Reanalysis Data Sets (CFSv2, MERRA, MERRA2, ERA-Interim, and NCEP/DOE R2) Used in This Study

	Data set				
	CFSv2	MERRA	MERRA 2	ERA-Interim	NCEP/DOE R2
Variable	Zonal wind ( $U$ ), meridional wind ( $V$ ), and temperature ( $T$ )				
Period	14 December 2014 to 31 December 2016 (25 months)				
Temporal resolution	Four times a day (6 hr)				
Model resolution	T382	$0.5^\circ \times 0.667^\circ$	$0.5^\circ \times 0.625^\circ$	T255	T62
	64 levels	72 levels	72 levels	60 levels	28 levels
Available horizontal resolution	$0.5^\circ \times 0.5^\circ$	$1.25^\circ \times 1.25^\circ$	$0.5^\circ \times 0.625^\circ$	$1.5^\circ \times 1.5^\circ$	$2.5^\circ \times 2.5^\circ$
Available vertical resolution	37 levels (1 hPa)	42 levels (0.1 hPa)	42 levels (0.1 hPa)	37 levels (1 hPa)	17 levels (10 hPa)
Data assimilation	3DVAR	3DVAR, with incremental update	3DVAR, with incremental update	4DVAR	3DVAR

Note. CFSv2 = Climate Forecast System version 2; MERRA = Modern Era Retrospective Analysis for Research and Applications; ERA-Interim = European Centre for Medium-Range Weather Forecasts (ECMWF) Interim; and NCEP/DOE R2 = National Centers for Environmental Prediction/Department of Energy Reanalysis 2; 3DVAR = three-dimensional variational data assimilation; 4DVAR = four-dimensional variational data assimilation.

result, a strong vertical temperature gradient is formed in the low and middle stratosphere in spring. In austral summer (December to February), the temperature increases to approximately 245 K ( $-28^\circ\text{C}$ ).

The Brunt-Väisälä frequency  $N$  is calculated from  $N^2 = g\partial\ln\theta/\partial z$ , where  $g$  is the gravitational acceleration ( $9.81\text{ m/s}^2$ ) and  $\theta$  is the potential temperature. On average, the Brunt-Väisälä frequency in the stratosphere is approximately  $0.02\text{ s}^{-1}$ , which is about twice as high as that in the troposphere ( $0.01\text{ s}^{-1}$ ). The tropopause region is observed near  $z = 8\text{ km}$  from February to May with an abrupt static stability change. The large temperature gradient near the tropopause is less clear from June to November due to the significantly low temperature of the lower stratosphere. The actual tropopause height at JBS each month will be calculated using temperature and potential vorticity (PV) in section 2.3. High static stability is found not only near the tropopause but also near the surface from April to November. A strongly stable boundary layer, with the Brunt-Väisälä frequency of approximately  $0.03\text{ s}^{-1}$  near the surface, is induced by longwave radiative cooling during the period when solar insolation is absent (King, 1990), which prohibits convection and frontal activities during the permanent dark period. In the stratosphere, the downward progression of high static stability is observed in early spring, which has been recognized by many Antarctic climate studies (e.g., Pfenninger et al., 1999; Yoshiki et al., 2004; Yoshiki & Sato, 2000). This is related to the strong vertical temperature gradient shown in Figure 3c, which is formed by solar heating transmitted from the upper stratosphere to the cold lower stratosphere after the sun rises in spring (Pfenninger et al., 1999).

## 2.2. Comparisons Between Radiosonde Observations and Reanalysis Data

As mentioned above, poor representation of the SH polar stratosphere during winter and spring in global models has been reported by various recent results and compared with available observations. Therefore, in this section, we evaluate the ability of global reanalysis data to represent the wind and temperature fields of Antarctica from the surface to midstratosphere using the first radiosonde observations conducted at JBS.

In the present study, four global reanalysis data sets are used: the Climate Forecast System version 2 (CFSv2; Saha et al., 2010, 2014) data set from the National Centers for Environmental Prediction (NCEP), the Modern Era Retrospective Analysis for Research and Applications (MERRA) data set from the National Aeronautics and Space Administration (Rienecker et al., 2011), the European Centre for Medium-Range Weather Forecasts (ECMWF) Interim Reanalysis (ERA-Interim) data set (Dee et al., 2011), and the NCEP/Department of Energy Reanalysis 2 (DOE R2) data set (Kanamitsu et al., 2002). Because MERRA data were not available after February 2016, the MERRA-2 data are used from March to December in 2016 (Gelaro et al., 2017). The details of each data set are listed in Table 3.

Figure 4 shows the time-height cross-sections of the zonal wind ( $U$ ), meridional wind ( $V$ ), and temperature ( $T$ ) revealed in the radiosonde (same as Figures 3a–3c) compared with those from CFSv2, MERRA, ERA-Interim (ERA-I), and NCEP/DOE R2 (NCEP R2) at JBS. For comparison, the reanalysis data sets at the four nearest grid points surrounding JBS are interpolated over the location of JBS using a bilinear interpolation (Bracegirdle & Marshall, 2012). Because MERRA sets the gridded data to the missing value when the pressure level is lower than the topographic height, the MERRA data are not shown near the surface in Figure 4. The daily as well as

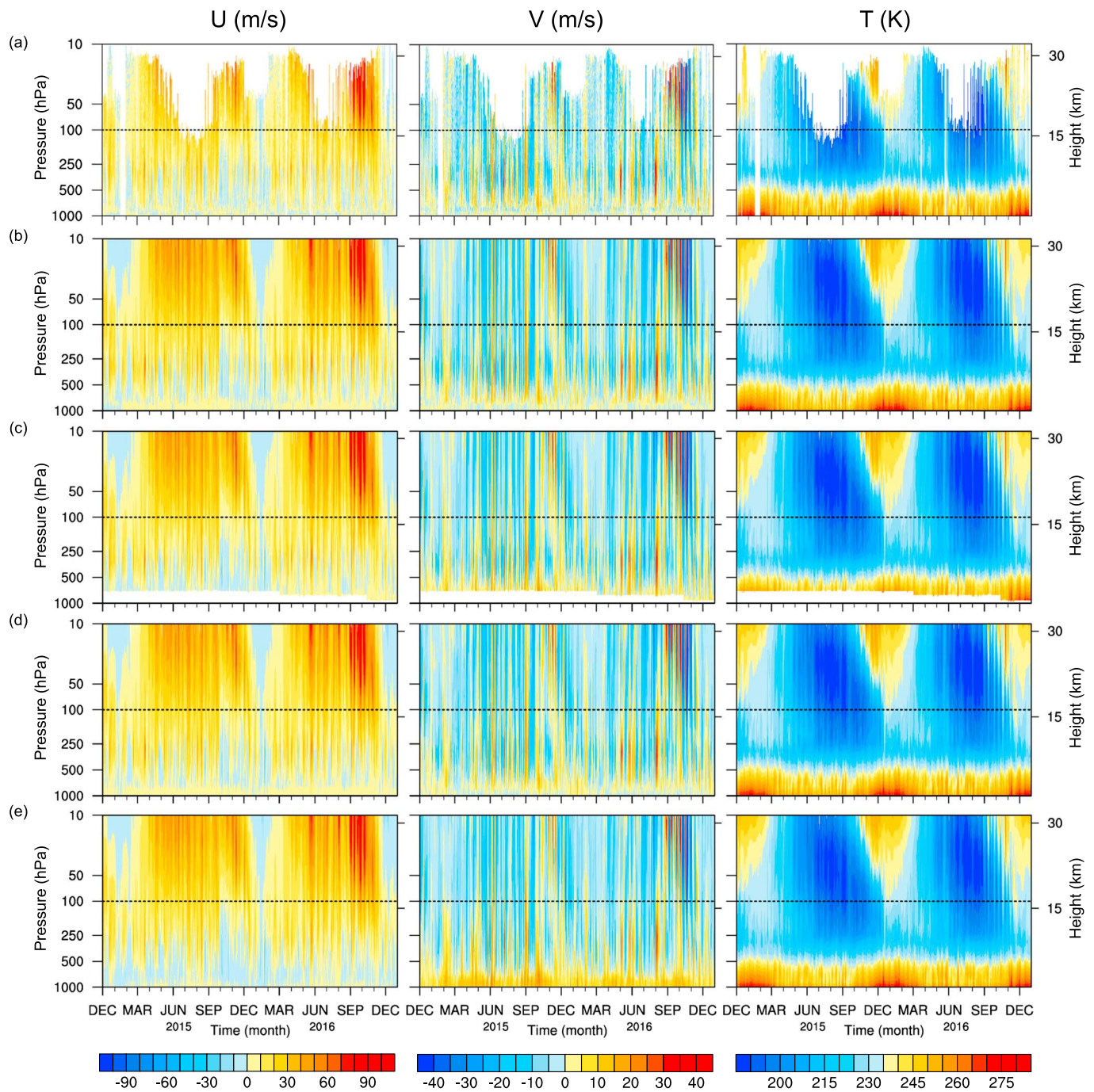


**Figure 4.** Time-height cross sections of the zonal wind ( $U$ ; first column), meridional wind ( $V$ ; second column), and temperature ( $T$ ; third column) revealed in the (a) radiosonde observations and the four reanalysis data sets at Jang Bogo Station: (b) Climate Forecast System version 2, (c) Modern Era Retrospective Analysis for Research and Applications, (d) European Centre for Medium-Range Weather Forecasts Interim Reanalysis, and (e) National Centers for Environmental Prediction/Department of Energy Reanalysis 2. The dotted line represents 100 hPa for an easier comparison.

annual variations in the wind and temperature fields from the four reanalyses generally agree with those from the radiosonde observations. In addition, the severe polar night jet from winter to spring and the significantly decreased temperature in the stratosphere during winter are represented well in the four reanalyses. However, in the lower troposphere (below 800 hPa), the zonal wind in CFSv2 and ERA-I are less variable than those in the observations, and that from NCEP R2 is mostly easterly with a relatively smaller magnitude than the observations. Meridional winds from NCEP R2 are significantly biased as southerly,



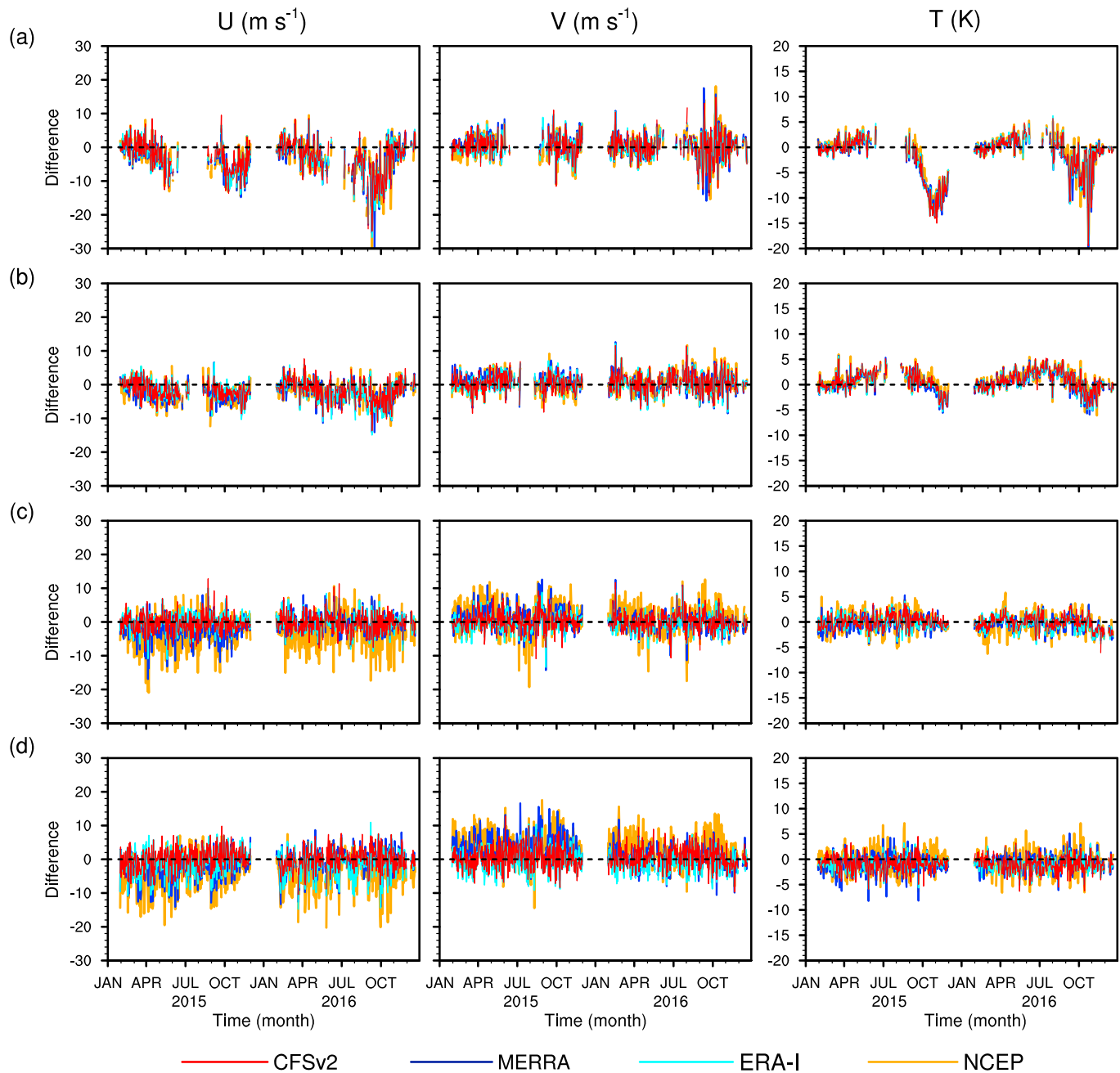


**Figure 5.** Differences in the zonal wind ( $U$ ; first column), meridional wind ( $V$ ; second column), and temperature ( $T$ ; third column) between the radiosonde observations and the four reanalysis data sets at (a) 50, (b) 100, (c) 500, and (d) 700 hPa. The red, blue, cyan, and orange lines represent the CFSv2, MERRA, ERA-Interim, and NCEP/DOE R2 data sets, respectively. CFSv2 = Climate Forecast System version 2; MERRA = Modern Era Retrospective Analysis for Research and Applications; ERA-Interim = European Centre for Medium-Range Weather Forecasts Interim Reanalysis; NCEP/DOE R2 = National Centers for Environmental Prediction/Department of Energy Reanalysis 2.

even when northerlies appear in the radiosondes, which are different from those in the other two reanalyses (CFSv2 and ERA-I) and the observations. Such uncertainties in the winds near the surface are likely due to the model's incomplete representation of the complex topography surrounding JBS (e.g., the coastal line of the Ross Sea and the steep downslope of the Transantarctic Mountains). For models with coarse horizontal resolutions, it is difficult to represent low-level winds above complex topographies (Elvidge et al., 2016). Furthermore, the terrain height for the four model grids surrounding JBS (~800 m) is considerably higher than the altitude of the JBS location (36 m); thus, the interpolation of reanalysis data over JBS may lead to

**Table 4**

*Bias, RMSE, and Correlation Coefficient for the Zonal Wind (U), Meridional Wind (V), and Temperature (T) Between the Radiosonde Observations at JBS and the Reanalyses That Are Interpolated Based on the Observations at Each Level*

Var	Product	Bias				RMSE				Correlation coefficient			
		Level (hPa)											
		700	500	100	50	700	500	100	50	700	500	100	50
U (m/s)	CFSv2	0.12	-0.35	-1.78	-2.94	3.12	2.76	3.37	5.7	0.89	0.95	0.97	0.97
	MERRA	-1.37	-1.01	-2.27	-3.58	4.16	3.38	3.72	6.15	0.81	0.93	0.97	0.97
	ERA-I	-1.08	-0.23	-1.94	-3.42	3.91	2.65	3.58	6.11	0.84	0.95	0.96	0.97
	NCEP	-4.06	-2.91	-2.26	-3.67	6.32	5.57	3.8	6.28	0.69	0.83	0.96	0.97
V (m/s)	CFSv2	0.62	0.15	0.51	0.36	3.31	2.63	2.74	3.56	0.82	0.95	0.95	0.95
	MERRA	1.54	0.47	0.77	0.57	4.09	3.09	2.79	3.6	0.78	0.93	0.95	0.95
	ERA-I	-0.46	-0.18	0.36	0.12	3.33	2.67	2.73	3.41	0.81	0.95	0.95	0.96
	NCEP	3.52	1.37	0.62	0.17	5.58	4.48	2.91	3.75	0.7	0.86	0.95	0.95
T (K)	CFSv2	-0.92	-0.02	0.69	-1.6	1.78	1.28	2.02	4.38	0.96	0.98	0.99	0.97
	MERRA	-0.85	-0.37	0.45	-1.7	1.86	1.44	1.97	4.38	0.95	0.97	0.99	0.97
	ERA-I	-1.05	-0.2	0.53	-1.56	1.72	1.38	1.96	4.35	0.97	0.97	0.99	0.97
	NCEP	-0.61	-0.28	0.84	-1.13	2.24	1.95	2.00	4.2	0.92	0.94	0.99	0.97

Note. RMSE = root mean square error; JBS = Jang Bogo Station; CFSv2 = Climate Forecast System version 2; MERRA = Modern Era Retrospective Analysis for Research and Applications; ERA-I = European Centre for Medium-Range Weather Forecasts (ECMWF) Interim Reanalysis; and NCEP = National Centers for Environmental Prediction.

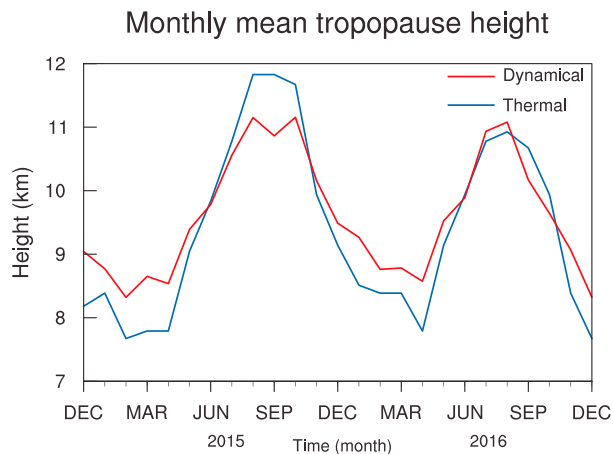
biases near the surface. Abovementioned differences between the observation and reanalysis data sets are shown in Figure S2.

Figure 5 shows the differences (reanalyses minus observations) between the observations and reanalyses for zonal wind, meridional wind, and temperature at four selected pressure levels representing the lower troposphere (700 hPa), middle troposphere (500 hPa), lower stratosphere (100 hPa), and middle stratosphere (50 hPa). For this comparison, radiosonde data are vertically interpolated onto the selected pressure levels, while the reanalyses data sets are spatially interpolated using the nearest four grids following the horizontal drift of ascending balloons that are vertically interpolated onto the pressure levels (Figure 2). Note that the GPS information for the MZS balloon is missing; thus, radiosonde data collected exclusively at JBS for 2 years from January 2015 to December 2016 are used for this validation. The statistics of average annual bias, root mean square error (RMSE), and correlation coefficient for the wind and temperature between the radiosonde observations and reanalyses are shown in Table 4.

In the lower troposphere (700 hPa), NCEP R2 has a significant underestimation of zonal wind and overestimation of meridional wind, with the largest RMSEs compared to the other reanalyses (Table 4). Those wind biases continue to 500 hPa, though with relatively smaller RMSEs than those at 700 hPa. The MERRA winds also have significant biases, with patterns similar to those observed in NCEP R2 until February 2016; however, these biases disappear after February 2016 in the MERRA-2 data set, which has a higher horizontal resolution (0.5° by 0.625°) compared to that of MERRA (1.25° by 1.25°). Although CFSv2, which has the highest horizontal resolution, exhibits generally weak biases in wind in the troposphere, the horizontal resolution is not likely the only factor for more realistic representation of wind and temperature from each reanalysis data set, especially in the troposphere where various physical processes are involved. For example, biases in the zonal wind from ERA-I (-1.08 m/s) and MERRA (-1.37 m/s) are comparable, although the horizontal resolution of ERA-I is coarser than that of MERRA. For the tropospheric temperature, all models exhibit negative temperature biases ranging from -1.05 to 0.02 K and very good correlations to the radiosonde observations.

In the stratosphere, the zonal wind is largely underestimated from the reanalyses, with significant seasonal variations in its biases (i.e., large biases from April to November and weak biases from December to March). This tendency is more evident at 50 hPa than at 100 hPa. A considerably large difference between the observation and the reanalyses of approximately 30 m/s appears at 50 hPa on 16 September 2016, which leads to a high RMSE greater than 6 m/s. The zonal wind biases from the reanalyses are likely larger when the observed zonal winds are stronger.

On the other hand, meridional winds in the stratosphere tend to be overestimated slightly without a noticeable seasonal preference, except for a strong underestimation of -16 m/s at 50 hPa revealed on 16



**Figure 6.** Tropopause height above Jang Bogo Station from December 2014 to December 2016, which is calculated using model-level European Centre for Medium-Range Weather Forecasts Interim Reanalysis data.

September 2016. Overall, the reanalyses do not represent strong winds (i.e., greater than 20 m/s) sufficiently well. The temperature bias in the stratosphere also has distinct seasonal variations (i.e., large negative biases from September to November, negligible biases from December to March, and small positive biases from April to August). Warm biases occur mostly during the wintertime after sunset, implying that the reanalyses overestimate the minimum temperature. On the other hand, cold biases occur across the entire temperature range in early spring due to the delayed spring warming in all models. The relationships between the biases and magnitude of each variable are described in Figure S3 and Text S2. The cold biases are consistent with the cold pole problem in the stratosphere in spring that was reported in Garcia et al. (2017). Given that polar temperatures determine the amount of ozone in models, the underestimation of temperature can cause unrealistic ozone loss in the polar stratosphere during spring.

To construct better reanalysis data, more observational data in polar regions should be assimilated. In fact, JBS has been a registered radiosonde station of the World Meteorological Organization (WMO) since November 2015 (<https://ruc.noaa.gov/raobs/>); the current data may have been assimilated in some reanalysis data sets used in the present study, although it has not been confirmed whether the WMO collected the raw data used in this study. Nevertheless, the evaluation results shown in Figures 5, S2, and S3 demonstrate the general problems of global models regarding wind and temperature in the SH polar region.

November 2015 (<https://ruc.noaa.gov/raobs/>); the current data may have been assimilated in some reanalysis data sets used in the present study, although it has not been confirmed whether the WMO collected the raw data used in this study. Nevertheless, the evaluation results shown in Figures 5, S2, and S3 demonstrate the general problems of global models regarding wind and temperature in the SH polar region.

### 2.3. Extraction of IGWs

The characteristics of IGWs revealed in radiosonde data are investigated in two atmospheric layers representing the troposphere and lower stratosphere to remove the effect of the tropopause where temperature and wind change abruptly. Because the tropopause height is less evident during wintertime (Figure 3d), we need to identify the location of the tropopause above JBS to determine the analysis layers. There are generally two ways to calculate the tropopause height. In this study, based on WMO (1957), the thermal tropopause height is defined as the lowest level at which the vertical temperature gradient decreases to 2 K/km or less and the average lapse rate at all higher levels within 2 km above this level does not exceed 2 K/km. The dynamical tropopause height is defined, following Zängl and Hoinka (2001), as the lowest level at which the PV increases to 3.5 PVU (1 PVU =  $10^{-6} \text{ K}\cdot\text{m}^2\cdot\text{kg}^{-1}\cdot\text{s}^{-1}$ ) and the mean potential vorticity between the tropopause and all higher levels within 2 km above the tropopause remains above 3.5 PVU. Applying both criteria, we calculate the tropopause height at JBS using the model-level ERA-I temperature and relative vorticity data. The model-level data, which have a vertical resolution twice that of the interpolated pressure-level reanalysis data sets (Kim & Chun, 2015), are more appropriate to calculate the vertical gradient temperature and vorticity when determining the tropopause.

Figure 6 shows the monthly mean dynamical and thermal tropopause heights over JBS. The monthly mean dynamical (thermal) tropopause height ranges from approximately 8–9 km (7–8 km) in summertime to 11–12 km (11–12 km) in wintertime. The annual cycle of the tropopause height agrees well with Zängl and Hoinka (2001), who showed a single-wave pattern for the tropopause height over the whole Antarctic region, with the highest pressure in summer and the lowest pressure in winter. Because the thermal tropopause height tends to have an exceptionally higher value in winter in Antarctica due to the small lapse rate that corresponds to a significantly cold lower stratosphere (Zängl & Hoinka, 2001), the dynamical tropopause height is used as the standard in wintertime. The analysis layers for the troposphere and stratosphere are determined as the altitudinal regions of 2–7 and 15–22 km, respectively, as the climatological tropopause layer thickness ranges from ~7.5 km in summer months (DJF) to ~5 km in winter months (JJA) over the South Pole (Feng et al., 2012). The lower limit of the troposphere is set to 2 km above the surface to avoid erroneous perturbation effects near the planetary boundary layer, and the upper limit of the stratosphere (22 km) is chosen to have a sufficient number of soundings to obtain statistically reasonable results. The selection of the upper limit of the tropospheric layer as 7 km is likely to be reasonable, considering that 7 km is just below the lowest calculated tropopause height. The lower limit of the stratospheric layer

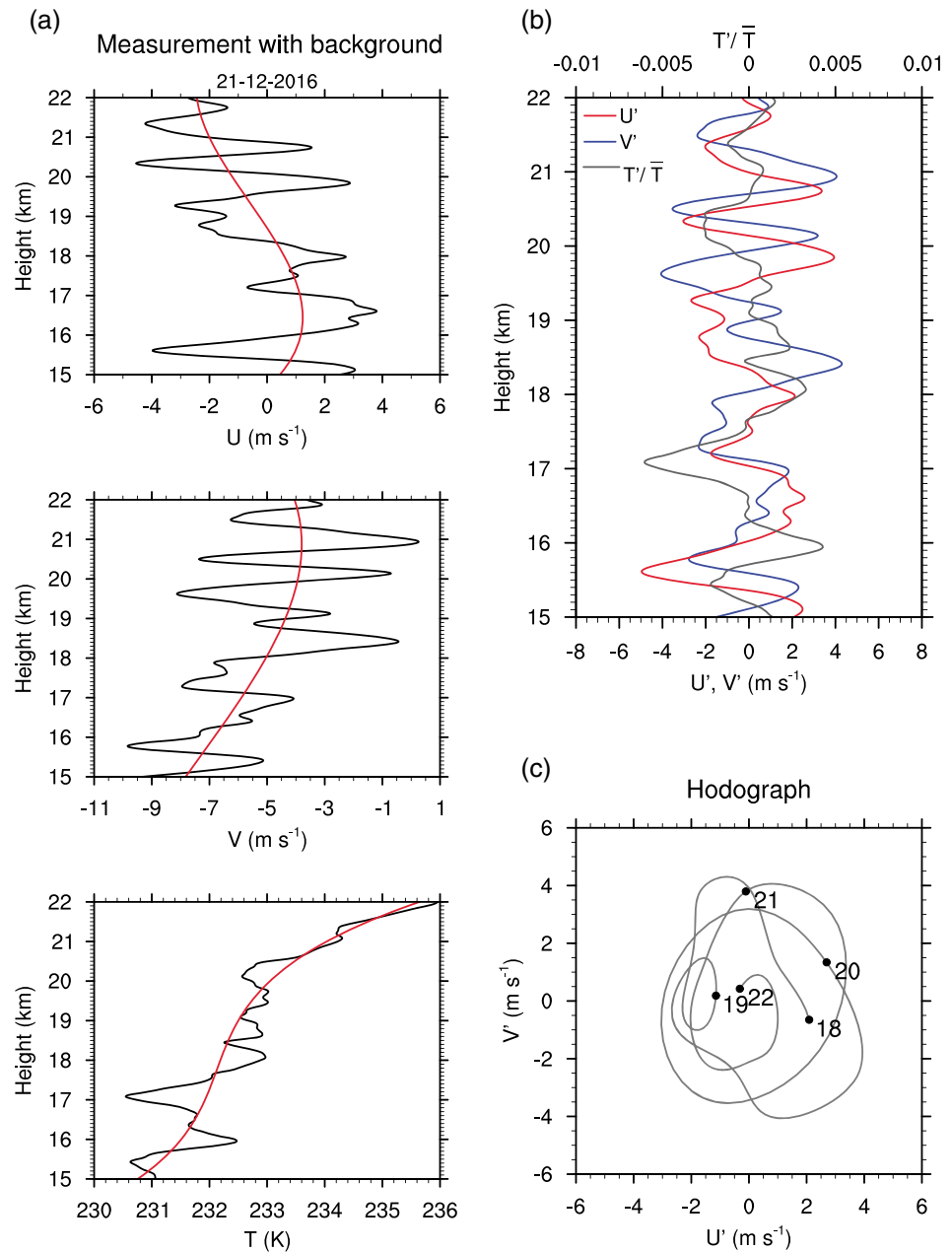


**Figure 7.** Sample (a) zonal wind (first row), meridional wind (second row), and temperature (third row) profiles displaying the interpolated data (black line) and background profiles (red line). (b) Differences (the red, blue, and gray lines denote the perturbations in the zonal wind, meridional wind, and normalized temperature, respectively) between the interpolated profiles and background profiles. (c) Hodograph of the wind perturbations in the stratosphere on 1 February 2015.

(15 km) is somewhat higher, which can reduce the depth of the stratosphere and, consequently, reduce the long wavelength components of GWs (Ki & Chun, 2011); however, it is determined to safely avoid some disturbances in the tropopause layer that covers over 2–3 km vertically from the tropopause. Considering that the tropopause height in winter and spring is approximately 12 km (Figure 6), a stratospheric layer starting at  $z = 15$  km is reasonable, while this height is likely too high in summer and autumn. For simplicity, in the present study, we use the same height range for the tropospheric layer and stratospheric layer without seasonal variations. Based on this setting, 727 (99%) soundings among a total of 729 profiles are used for the tropospheric analyses, while 554 (75%) soundings that reached up to 22 km are used for the stratospheric analyses (Table 2).

The GW components are defined by wind and temperature perturbations ( $u'$ ,  $v'$ , and  $T'$ ), which are obtained by subtracting the basic-state profiles ( $\bar{u}$ ,  $\bar{v}$ , and  $\bar{T}$ ) from the observed profiles. In this study, the basic state is determined for each analysis layer by fitting a third-order polynomial using the least square method following Vincent et al. (1997). As an example, Figure 7 illustrates the observed zonal wind, meridional wind, and temperature profiles (black lines) superimposed on their basic-state profiles (red curves, Figure 7a). The wind perturbations and normalized temperature perturbations are also shown (Figure 7b), along with a hodograph of the wind perturbations (Figure 7c) in the stratospheric layer at 00 UTC on 1 February 2015. As shown in Figure 7a, the polynomial fit represents the smoothly varying vertical profile of a large-scale feature, which satisfies the Wentzel-Kramers-Brillouin approximation to be used in the GW theory. Wind and temperature perturbations in Figure 7b exhibit clear wave-like structures with vertically varying amplitudes, with maximum perturbations of 4 m/s for the winds and 0.0014 for the normalized temperature. The dominant vertical wavelength for the wind perturbations is approximately 1.5 km. The zonal wind perturbation has a phase lag with the meridional wind perturbation of one fourth of a cycle above  $z = 18$  km, whereas this relationship is less evident below that height. The elliptical shape of the hodograph (Figure 7c) is also apparent in the region of 18–22 km, and the perturbation wind vectors rotate anticyclonically (anticlockwise [ACW] rotation in the SH) with height, implying upward-propagating IGWs. Considering the presence of multiple waves in a profile, the recent GW studies (Moffat-Griffin et al., 2011; Moffat-Griffin & Colwell, 2017; Murphy et al., 2014) employ the wavelet analysis method (Zink & Vincent, 2001) to identify the individual GWs. Although the wavelet technique allows to isolate the individual waves in the wave packets, unlike the method of Vincent et al. (1997), which is based on the monochromatic wave theory, the use of Morlet wavelet in the wavelet technique limits the maximum resolvable vertical wavelength to be less than fifth of the depth of the analysis layer, given that it can only contain about five cycles in its Gaussian envelope. Considering that the depth of analysis layer (5 km in the troposphere and 7 km in the stratosphere) is somewhat shallow, the vertical wavelength resolved from the wavelet technique will be less than 1 km (2 km) in the troposphere (stratosphere). Therefore, we used the method by Vincent et al. (1997) in the present study.

To identify IGWs from the observed perturbations, we first examine whether they satisfy the polarization relation by calculating the degree of polarization ( $dp$ ) using the Stokes parameter spectra method following Eckermann (1996). Stokes parameters  $I$ ,  $D$ ,  $P$ , and  $Q$  are calculated as

$$I = \int_m |\hat{u}(m)|^2 + |\hat{v}(m)|^2, \quad (1)$$

$$D = \int_m |\hat{u}(m)|^2 - |\hat{v}(m)|^2, \quad (2)$$

$$P = \int_m 2 \operatorname{Re}[\hat{u}^*(m)\hat{v}(m)], \quad (3)$$

$$Q = \int_m 2 \operatorname{Im}[\hat{u}^*(m)\hat{v}(m)]. \quad (4)$$

Here  $I$  is the throughput parameter,  $D$  is the throughput anisotropy parameter,  $P$  is the linear polarization parameter,  $Q$  is the circular polarization parameter,  $\hat{u}$  and  $\hat{v}$  are the Fourier coefficients for the zonal and meridional wind perturbations, respectively, and the superscript \* represents the complex conjugate. Using the above formulations, we define  $dp$  as

$$dp = \frac{(D^2 + P^2 + Q^2)^{\frac{1}{2}}}{I}, \quad (5)$$

where  $0 \leq dp \leq 1$ . When  $dp = 1$ , the polarization relationship between the horizontal wind perturbations of IGW is perfectly satisfied, while  $dp = 0$  indicates that there is no polarization relationship for IGW. Hence, perturbations with a  $dp$  greater than 0.5 are regarded as coherent IGWs. The axial ratio (AXR; the ratio of the minor axis to the major axis) of a hodograph, which is equivalent to the Coriolis parameter divided by the intrinsic frequency ( $f/\hat{\omega}$ ), is calculated using the Stokes parameters (Eckermann & Vincent, 1989) by

$$\text{AXR} = \tan(\zeta), \quad (6)$$

$$\zeta = \frac{1}{2} \arcsin\left(\frac{Q}{\sqrt{D^2 + P^2 + Q^2}}\right), \quad (7)$$

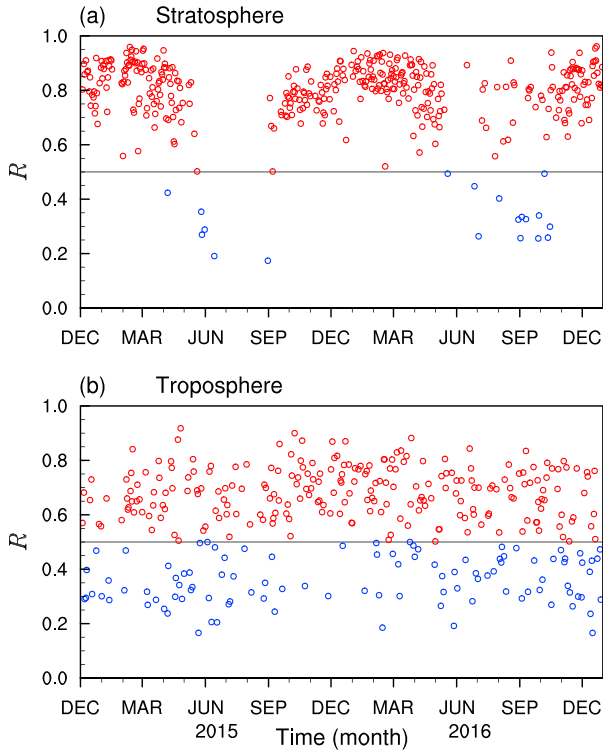


**Figure 8.** Time series of the rotary ratio ( $R$ ) of the anticlockwise rotating component to the total rotating components (anticlockwise + clockwise) for each observed wave in the (a) stratosphere and (b) troposphere. The black lines across the graphs represent the 0.5 value. The red (blue) circles denote upward (downward) propagating waves with  $R$  values greater (less) than 0.5.

Considering the transverse-shear effect (Hines, 1989), we can calculate the intrinsic frequency using the corrected axial ratio ( $AXR_{corr}$ ), which is defined as

$$AXR_{corr} = \left| AXR - \frac{1}{N} \frac{dV_T}{dz} \right|, \quad (8)$$

where  $V_T$  is the mean wind transverse to the propagation direction. The intrinsic frequencies higher than a certain value are less reliable, because the errors in wind measurement limit the accuracy of  $AXR$ , and thus, they should be excluded when calculating the average value of wave parameters (Vincent & Alexander, 2000). Given that the average of the root mean square wind perturbation is 1.58 and 2.50 m/s in the troposphere and stratosphere, respectively, the cutoff intrinsic frequency, which is determined from the root mean square wind perturbation divided by the accuracy of wind measurement (0.15 m/s in Table 1), is approximately  $10.5f$  and  $16.6f$  in the troposphere and stratosphere, respectively. However, we used a fixed value of  $10f$  as the upper limit of the intrinsic frequency in both the troposphere and the stratosphere, to make a consistent analysis in the two layers. Note that there are only six profiles in the stratosphere with the intrinsic frequencies ranging between  $10f$  and  $16f$ . Therefore, in the present study, only the profiles with the intrinsic frequency in a range of  $f < \hat{\omega} \leq 10f$  are selected. Among the 727 and 554 profiles in the troposphere and stratosphere, respectively, 334 (46%) profiles in the troposphere and 387 (70%) profiles in the stratosphere that satisfy both conditions are used for the analyses in the present study. The number of available soundings satisfying these conditions each month is listed in Table 2.

### 3. Results

#### 3.1. Vertical Propagation of IGWs

The horizontal wind vector of IGW rotates ACW (clockwise [CW]) with height in the SH ( $f < 0$ ) for upward (downward) energy propagation. The rotation of IGWs can be estimated quantitatively by calculating the rotary spectrum (Vincent, 1984), which decomposes the wave motions into ACW and CW rotating components. Although the rotary spectral analysis tends to underestimate the percentage of upward-propagating waves as  $\hat{\omega}/f$  increases (Wang et al., 2005), we use this method given that most of the observed IGWs have low frequencies, with  $\hat{\omega}$  less than  $4f$  (which will be shown later).

Figure 8 illustrates the rotary ratio ( $R$ ), which is calculated by  $ACW/(CW + ACW)$  for IGWs. In this study, the vertical propagation direction of IGWs is defined as *upward* when the rotary ratio is greater than 0.5 and *downward* when the ratio is less than 0.5. In the stratosphere, upward-propagating (up-going hereafter) IGWs are more prevalent than downward-propagating (down-going hereafter) ones. The number of down-going IGWs increases from late autumn to early spring (April to September in 2015 and May to October in 2016) and is accompanied by a decrease in up-going waves. This is consistent with the results from previous studies at several radiosonde stations in Antarctica (e.g., Murphy et al., 2014, at Davis Station, Sato & Yoshiki, 2008, at Syowa Station, and Moffat-Griffin et al., 2011, at Rothera Station) over a similar period (from May to October). The down-going IGWs in the stratosphere are likely generated during the process of a flow imbalance, which is associated with polar night jets in the upper stratosphere (Murphy et al., 2014; Plougonven & Zhang, 2016; Sato & Yoshiki, 2008). To assess this possibility, the residual of the nonlinear balance equation (hereafter *RNBE*), which represents the flow imbalance associated with jet/frontal system (Zhang, 2004), is calculated using 6-hourly ERA-Interim data. *RNBE* in the spherical coordinates is defined as follows (Chun et al., 2014):

$$RNBE = 2J(u, v) + f\zeta - \nabla^2\Phi - \beta u + X - D^2 - \frac{\partial \vec{V}}{\partial P} \cdot \vec{\nabla} \omega, \quad (9)$$

$$X = \frac{(u^2 + v^2) \tan^2 \phi}{a^2} - \frac{u^2 + v^2}{a^2 \cos^2 \phi} - \frac{2 \tan \phi}{a^2} \left( u \frac{\partial u}{\partial \phi} + v \frac{\partial v}{\partial \phi} \right), \quad (10)$$

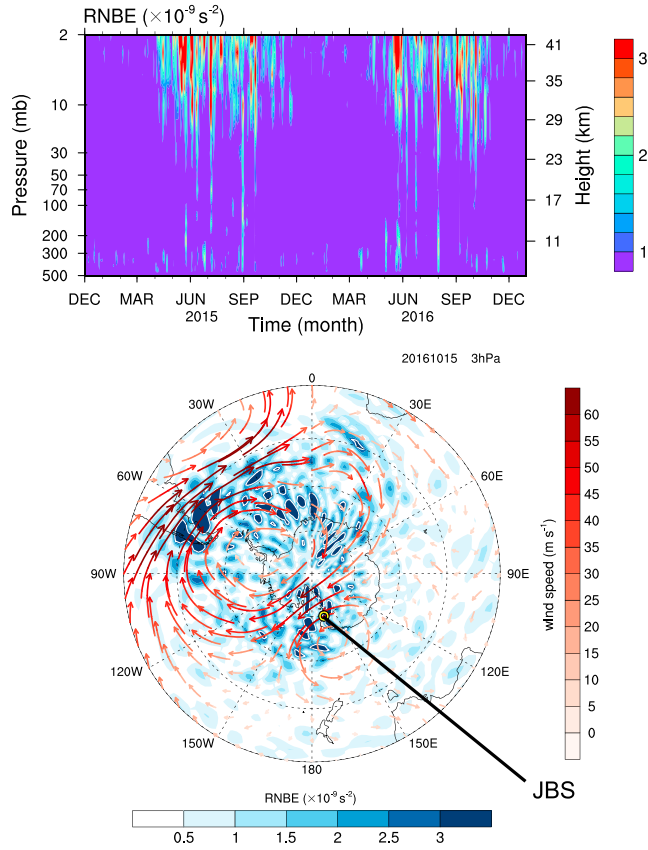


**Figure 9.** (a) Time-height cross section of  $|RNBE|$  above JBS during the data period. (b) Polar stereographic projection maps of the horizontal wind vector superimposed on  $|RNBE|$  (shading) at 3 hPa on 15 October 2016. Yellow circle denotes the location of JBS. JBS = Jang Bogo Station.

(Yoshiki et al., 2004) can generate down-going IGWs into the troposphere and up-going IGWs into the stratosphere. The overall features of the vertical propagation statistics in the troposphere and stratosphere in the current study are consistent with those from Pfenninger et al. (1999) (see Figure 12). In the present study, analyses of the observed IGWs are conducted by dividing the up-going and down-going waves separately.

### 3.2. Horizontal Propagation of IGWs

The intrinsic phase velocity ( $\hat{c}$ ), ground-based phase velocity ( $\hat{c}$ ), and ground-based group velocity ( $c_g$ ) are calculated by

$$\hat{c} = \hat{\omega} \frac{k_h}{|k_h|^2}, \quad (12)$$

$$c = (\hat{\omega} + k_h \cdot V) \frac{k_h}{|k_h|^2}, \quad (13)$$

$$c_g = V + \hat{c}_g = V + \left(1 - \frac{f^2}{\hat{\omega}^2}\right) \hat{c}. \quad (14)$$

Here  $V$  is the vertically averaged basic-state horizontal wind vector and  $k_h = k_r(\cos \varphi, \sin \varphi)$  is the horizontal wavenumber vector, where  $\varphi$  represents the azimuth of the horizontal propagation of GWs, which is determined by  $\varphi = \tan^{-1}(y/x)$ , where  $x = \overline{u'T'_{+90}}$  and  $y = \overline{v'T'_{+90}}$ . Here  $T'_{+90}$  represents that all spectral components of  $T'$  are transformed by  $+90^\circ$  by the Hilbert transform (Vincent et al., 1997).

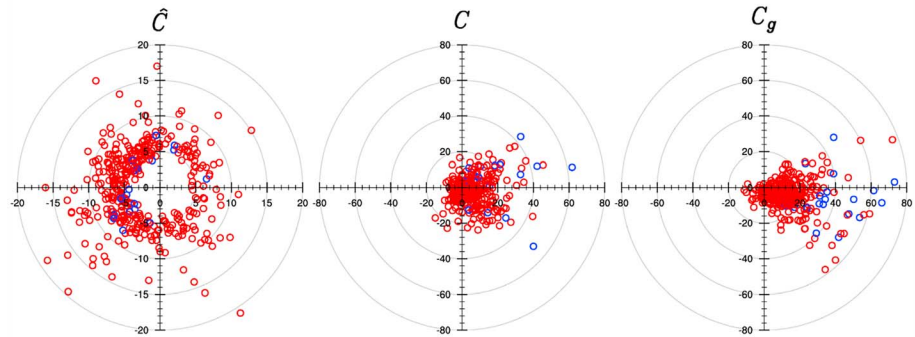
$$D^2 = \left(\nabla \cdot \vec{V}\right)^2 = \left(\frac{\partial u}{a \cos \phi \partial \lambda} + \frac{\partial(v \cos \phi)}{a \cos \phi \partial \phi}\right)^2. \quad (11)$$

Here  $J(u, v)$  is the Jacobian of  $u$  and  $v$ , where  $u$  is the zonal wind and  $v$  is the meridional wind.  $\zeta$  is the vertical component of relative vorticity,  $\Phi$  is the geopotential height,  $\beta = \partial f / \partial y$  is the meridional gradient of the Coriolis parameter,  $D$  is the divergence,  $P$  is air pressure,  $\omega$  is the vertical velocity,  $a$  is the radius of the Earth (approximately 6,371 km),  $\lambda$  is longitude, and  $\phi$  is latitude. A low-pass filter with cut-off zonal wavenumber 22 is applied to the reanalysis data to eliminate the grid-resolved GWs (Sato et al., 2009).

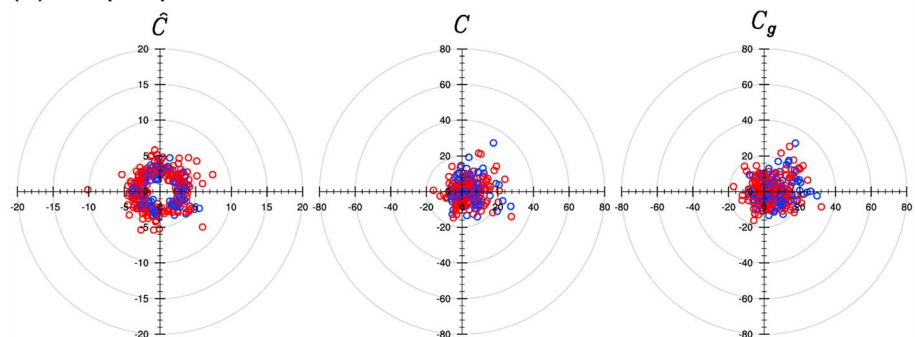
Figure 9a shows the vertical distribution of magnitude of  $RNBE$  above JBS up to 2 hPa. There is a strong enhancement of  $RNBE$  above 29 km from autumn to spring, which is consistent with the period when down-going IGWs appear in the lower stratosphere in Figure 8. Figure 9b presents a polar stereography of  $RNBE$  at 3 hPa on 15 October 2016 when down-going IGW is observed (Figure 8a). Considerably high  $RNBE$  exceeding  $3 \times 10^{-9} \text{ s}^{-2}$  occurred above JBS. For all the dates when down-going IGWs appear in the stratosphere (Figure 8a), relatively high  $RNBE$  is observed above the stratospheric analysis layer (15–22 km) over JBS. This implies that down-going IGWs are likely induced by the imbalance of flow associated with the polar night jet in the upper stratosphere. Details in the sources of the observed IGWs at JBS, including the polar night jet in the stratosphere, will be investigated in Part 2, using a three-dimensional ray-tracing model of IGWs.

In contrast to that in the stratosphere, the number of down-going IGWs is comparable to that of up-going IGWs in the troposphere without any temporal variation. This is somewhat expected, given that various sources in the lower troposphere can generate up-going IGWs into the troposphere and stratosphere, while sources in the upper troposphere associated with the tropospheric jet or instabilities in the large-scale flow

(a) Stratosphere



(b) Troposphere



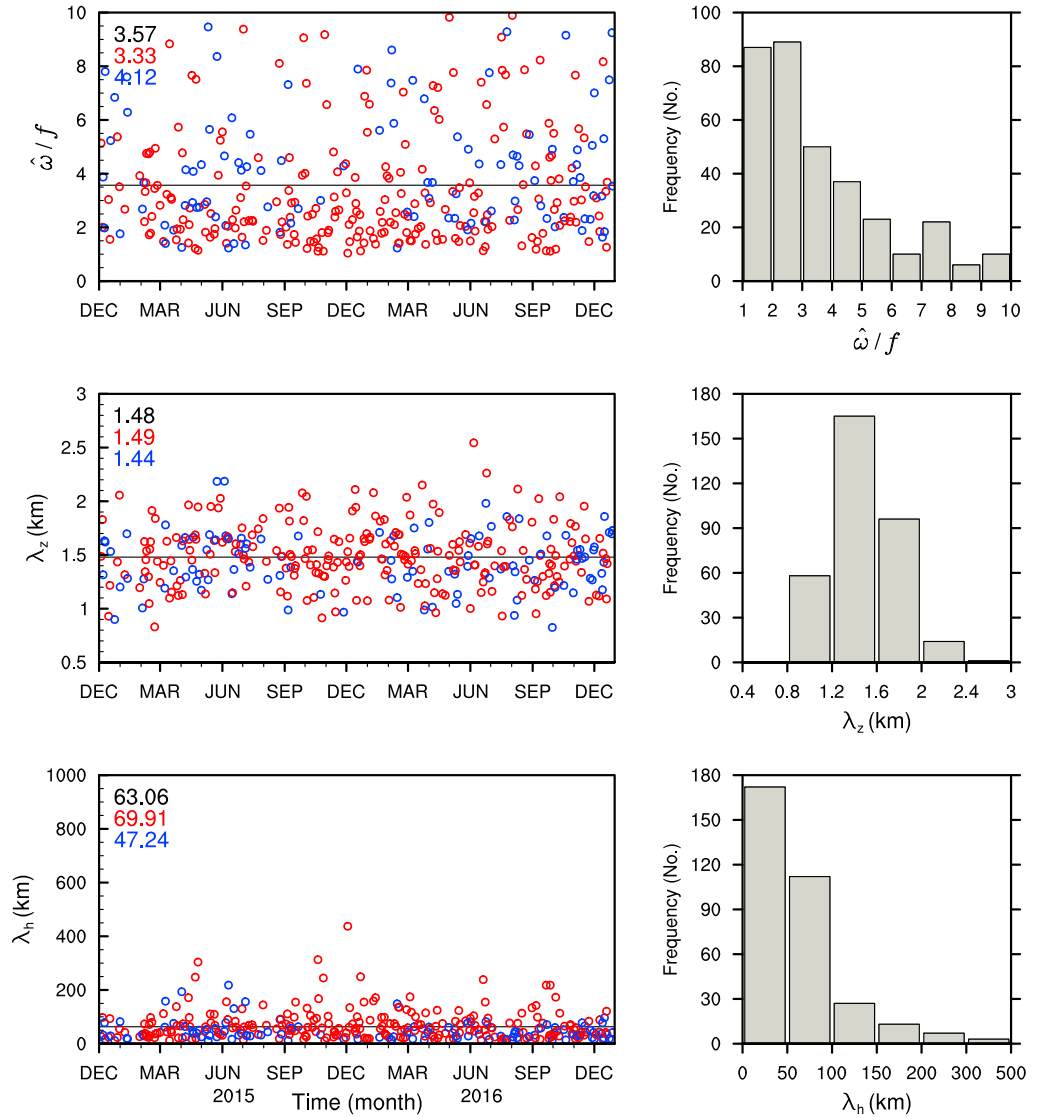
**Figure 10.** Distributions of the intrinsic phase velocity (first column), ground-based phase velocity (second column), and ground-based group velocity (third column) for each wave observed in the (a) stratosphere and (b) troposphere. The red and blue circles denote the upward and downward propagating waves, respectively.

Figure 10 shows the intrinsic phase velocity ( $\hat{c}$ ), the ground-based phase velocity ( $c$ ), and the ground-based group velocity ( $c_g$ ) of the observed IGWs at JBS. In the troposphere, the intrinsic phase velocity of both up-going and down-going IGWs is isotropic centered at zero, with a typical speed of approximately 2–4 m/s. In the stratosphere, on the other hand, a majority of up-going and down-going IGWs directs westward relative to the background wind. The intrinsic phase speeds are in the range of 4–8 m/s, which are relatively larger than those in the troposphere.

The ground-based phase velocities of both up-going and down-going IGWs in the troposphere direct westward as much as eastward, but the eastward propagating IGWs have a wider speed range ( $c = 0\text{--}40$  m/s) than that of the westward propagating IGWs ( $c = 0\text{--}20$  m/s). This is likely due to the fact that the tropospheric basic-state wind changes its direction frequently and the westerlies are somewhat stronger than the easterlies. In the stratosphere, the ground-based phase velocities direct mostly eastward, with a large phase speed range (approaching 70 m/s) due to prevailing westerlies. From the fact that many of up-going IGWs have positive ground-based phase velocities and negative intrinsic phase velocities under the dominant westerlies in the stratosphere, it can be deduced that IGWs with phase speeds less than the basic-state wind could propagate upward from the lower layer into the stratospheric analysis layer without being filtered.

As the background wind dominates the energy propagation of GWs, most of the ground-based group velocity direct east and southeast. The magnitude of the average horizontal group velocity (16.55 m/s in the stratosphere and 9.66/m s in the troposphere) is considerably greater than the average vertical group velocity (0.05 m/s in the stratosphere and 0.08 m/s in the troposphere), which indicates that IGWs, especially in the stratosphere, tend to travel further horizontally than vertically. This is consistent with the result reported in Murphy et al. (2014) that the GWs observed at Davis Station travel at an oblique angle from their source. Hence, IGWs in the stratosphere could be generated by sources far from JBS.





**Figure 11.** Scatter plots (left) and histograms (right) of the intrinsic frequency divided by the Coriolis parameter (upper), vertical wavelength (middle), and horizontal wavelength (lower) calculated for each wave observed in the troposphere and stratosphere. The red and blue circles denote upward and downward propagating waves, respectively. The black lines across the graphs represent the averages for each value regardless of the vertical propagation direction.

### 3.3. Intrinsic Frequency and Wavelengths

By using the dispersion relation, we obtain the horizontal wavenumber  $k_h$  using the intrinsic frequency calculated from equation (6) as

$$k_h^2 = \frac{m^2 f^2 [(\hat{\omega}/f)^2 - 1]}{N^2}, \quad (15)$$

where  $m$  is the vertical wavenumber, which is calculated by

$$m = \frac{\sum_i (|\hat{u}_i|^2 + |\hat{v}_i|^2) m_i}{\sum_i (|\hat{u}_i|^2 + |\hat{v}_i|^2)}. \quad (16)$$

Here  $\hat{u}_i$  and  $\hat{v}_i$  are the coefficients of the  $i$ th Fourier component corresponding to the  $i$ th vertical wavenumber  $m_i$ . The intrinsic frequency divided by the Coriolis parameter ( $\hat{\omega}/f$ ), the vertical wavelength, and the horizontal

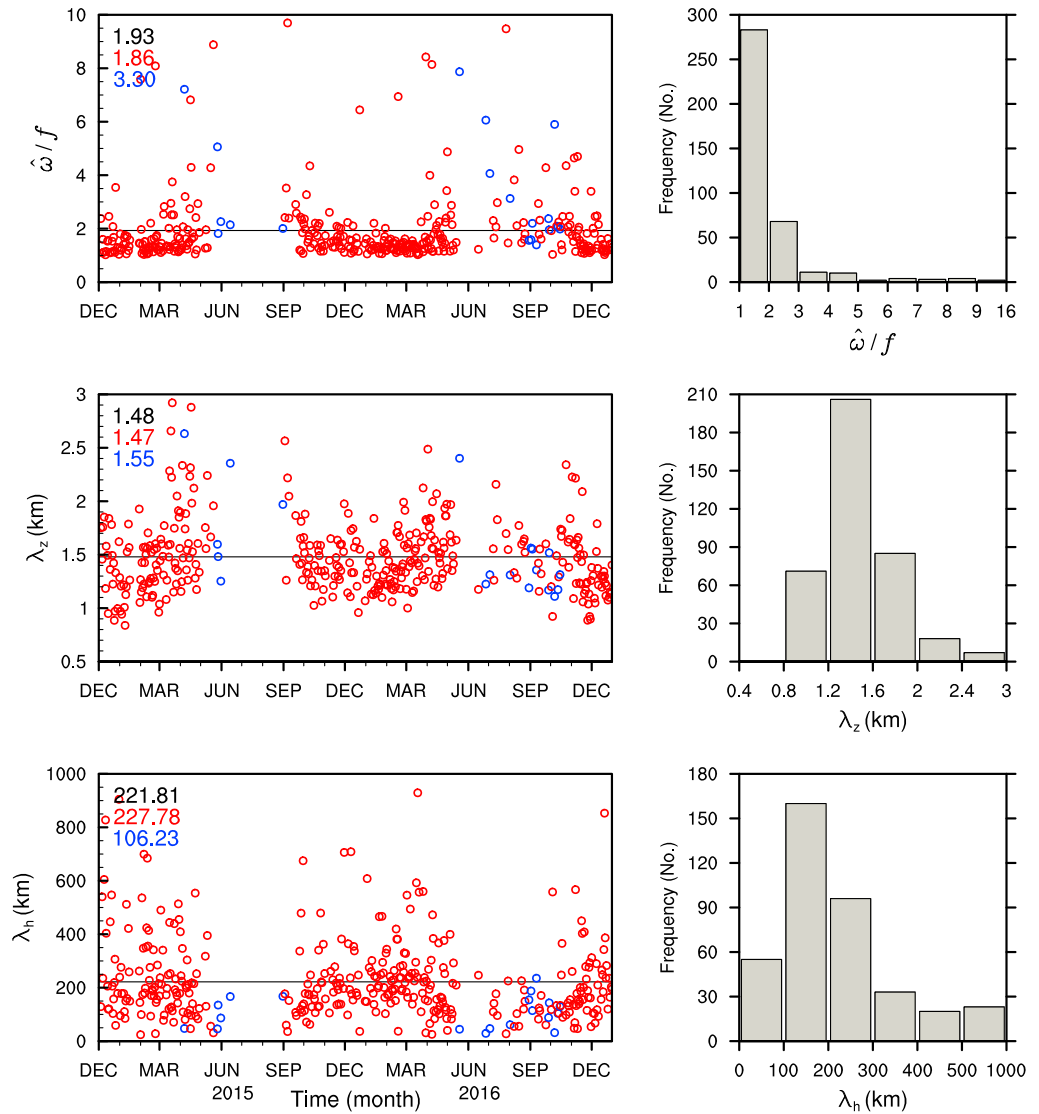


**Figure 12.** The same as Figure 11 but in the stratosphere.

wavelength of the observed IGWs in the troposphere (stratosphere) are depicted in Figure 11 (Figure 12). The numbers written in the upper-left corner of each panel denote the average value regardless of the vertical propagation direction (black) and that exclusively for the up-going IGWs (red) and that for the down-going IGWs (blue).

In the troposphere (Figure 11), both up-going and down-going IGWs exhibit a wider distribution of  $\hat{\omega}/f$ , with an average of 3.57 corresponding to a period of 3.49 hr. IGWs with a short vertical wavelength (approximately 1.5 km) are prevalent with an average value of 1.48 km. The horizontal wavelength calculated from equation (15) is primarily smaller than 200 km, with an average of 63.06 km. The averaged intrinsic frequency of the down-going IGWs is somewhat higher than that of up-going ones, while there are no remarkable differences in the intrinsic frequency. Thus, the averaged horizontal wavelengths of the down-going IGWs is shorter than those of up-going IGWs by the dispersion relation. There are not apparent seasonal variations.

In the stratosphere (Figure 12), an average  $\hat{\omega}/f$  for all waves is 1.93, and a corresponding period is 6.45 hr. Similar to the vertical wavelengths of IGWs revealed in the troposphere, IGWs in the stratosphere have a typical range of 1–2 km, with an average vertical wavelength of 1.48 km. Most of IGWs have a horizontal wavelength less than 500 km, with an average of 221.81 km. The intrinsic frequency and vertical wavelength in the stratosphere increase from autumn (MAM) to spring (SON) with a few of significantly higher values.

Corresponding horizontal wavelengths decrease (increase) significantly from March to September (October to February). The average horizontal wavelength in the stratosphere is roughly 3 times greater than that in the troposphere because the value of  $\bar{\omega}/f$  is reduced by a half, and the Brunt-Väisälä frequency is twice that in the troposphere. The up-going and down-going IGWs in the stratosphere have similar vertical wavelengths, but the intrinsic frequency of the down-going IGWs are relatively higher than that of up-going IGWs. Thus, the averaged horizontal wavelength of the down-going IGWs are shorter than that of the up-going IGWs by the dispersion relation. However, a direct comparison between the up-going and down-going IGWs is not feasible due to a much smaller number of down-going IGWs.

### 3.4. Wave Energy

GW activity is estimated by calculating the potential ( $E_P$ ), kinetic ( $E_K$ ), and total ( $E_T$ ) energies per unit mass, as defined by

$$E_P = \frac{1}{2} \left( \frac{g \overline{T'}}{N \overline{T}} \right)^2, \quad (17)$$

$$E_K = \frac{1}{2} \overline{u'^2 + v'^2}, \quad (18)$$

$$E_T = E_K + E_P. \quad (19)$$

Because  $\overline{u'}$  and  $\overline{v'}$  are much greater than the vertical velocity perturbation  $\overline{w'}$  (Innis et al., 2004),  $\overline{w'}$  is neglected when calculating the kinetic energy. Although  $\overline{w'}$  is estimated from the ascending rate of balloons, which has been done in previous studies (e.g., Innis et al., 2004; Lalas & Einaudi, 1980), these waves represent high-frequency internal GWs rather than IGWs considered in this study. The overbars in the equations denote a vertical average over the analysis layer. Figure 13 shows the scatterplots of  $E_K$ ,  $E_P$ ,  $E_T$ , and the ratio of the kinetic energy to the potential energy ( $E_K/E_P$ ), which is calculated for each observed sounding in the troposphere (Figure 13a) and stratosphere (Figure 13b). The numbers written in the upper-left corner of each panel denote the average values for all waves (black) and that exclusively for the up-going IGWs (red) and that for the down-going IGWs (blue).

The kinetic energy of IGWs from the individual soundings in the troposphere is primarily less than 5 J/kg, with an average of 1.42 J/kg, whereas that in the stratosphere is relatively large (3.27 J/kg), with extremely high values ( $>10$  J/kg). In contrast, the potential energy is generally similar in the troposphere and stratosphere, with average values of 1.36 and 1.14 J/kg, respectively. Although the amplitudes of  $\overline{u'}$ ,  $\overline{v'}$ , and  $\overline{T'}/\overline{T}$  increase with height due to the exponential decrease in density, the impact of the increase in  $\overline{T'}/\overline{T}$  (equation (17)) is largely canceled by the increase in the Brunt-Väisälä frequency in the stratosphere, resulting in comparable or even less potential energy in the stratosphere. Dominated by the kinetic energy, the total energy is larger in the stratosphere, with an average value of 4.41 J/kg, than in the troposphere (2.78 J/kg). The average of  $E_K/E_P$  in the stratosphere is 5.18, which is considerably higher than that in the troposphere (1.82). The average values for the down-going and up-going waves are generally similar to each other in the troposphere. In the stratosphere, both the average kinetic and potential energies for the down-going waves are relatively larger than those for the up-going waves. However, the average value of down-going waves is not statistically meaningful, as down-going waves are rare. Apparent seasonal variations in the total wave energy in the stratosphere are due to the relatively large kinetic energy and potential energy in autumn (MAM) and spring (SON) compared to those in summer (DJF), which is not evident in the troposphere.

### 3.5. GW Momentum Flux

The magnitude and sign of the momentum flux are important for estimating the contribution of GWs to the large-scale mean flow. The vertical fluxes of zonal ( $\overline{u'w'}$ ) and meridional ( $\overline{v'w'}$ ) momentum per unit mass (hereafter MF) can be estimated by

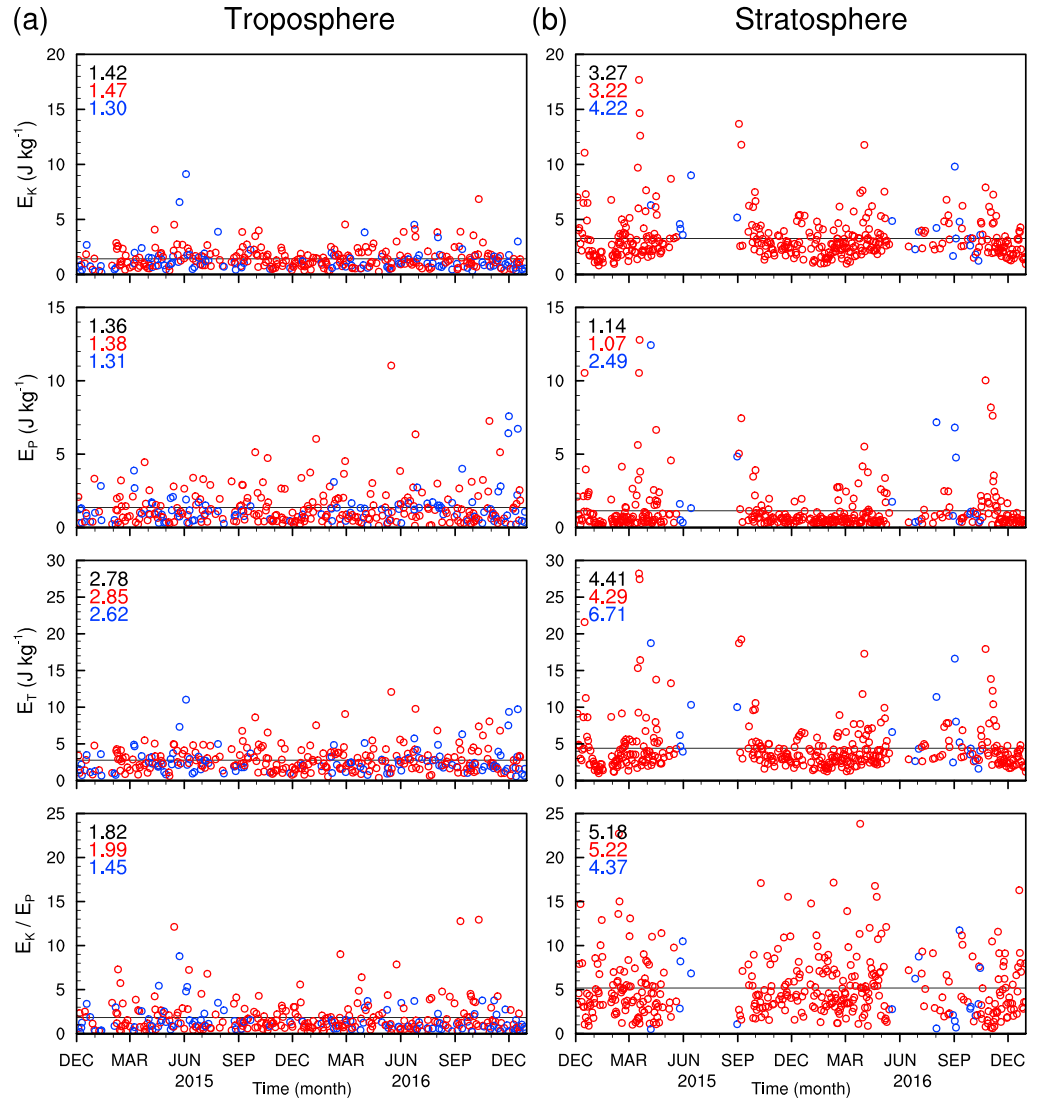


**Figure 13.** Scatter plots of kinetic energy (first row), potential energy (second row), total energy (third row) per unit mass, and the energy ratio (fourth row) for each wave observed in the (a) troposphere and (b) stratosphere. The black lines across the graphs represent the average for each value. The red and blue circles denote upward and downward propagating waves, respectively.

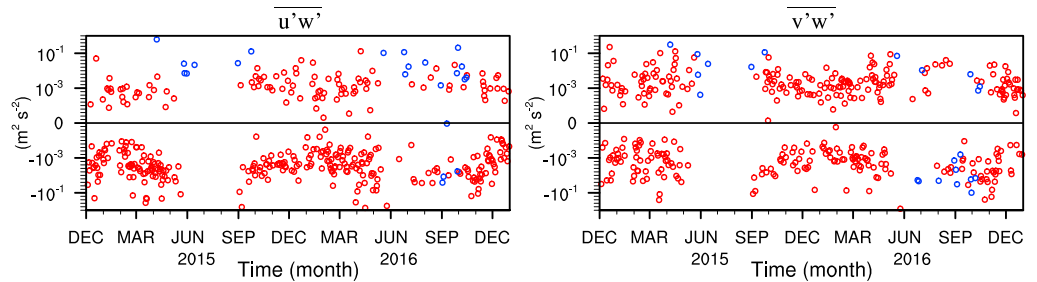
$$\overline{u'w'} = \frac{g\hat{\omega}}{N^2} \overline{u' \left( \frac{T'}{T} \right)_{+90}} \left[ 1 - \left( \frac{f}{\hat{\omega}} \right)^2 \right], \quad (20)$$

$$\overline{v'w'} = \frac{g\hat{\omega}}{N^2} \overline{v' \left( \frac{T'}{T} \right)_{+90}} \left[ 1 - \left( \frac{f}{\hat{\omega}} \right)^2 \right], \quad (21)$$

using the phase relationship between perturbations based on the monochromatic IGW theory (Vincent et al., 1997). Figure 14 presents the time series of the zonal and meridional MFs per unit mass averaged over each analysis layer.

In the stratosphere, the average zonal and meridional MFs are  $-0.008$  and  $-0.0005 \text{ m}^2/\text{s}^2$ , respectively. Both the zonal and meridional MFs for down-going waves are mostly positive, whereas up-going waves

(a) Stratosphere



(b) Troposphere

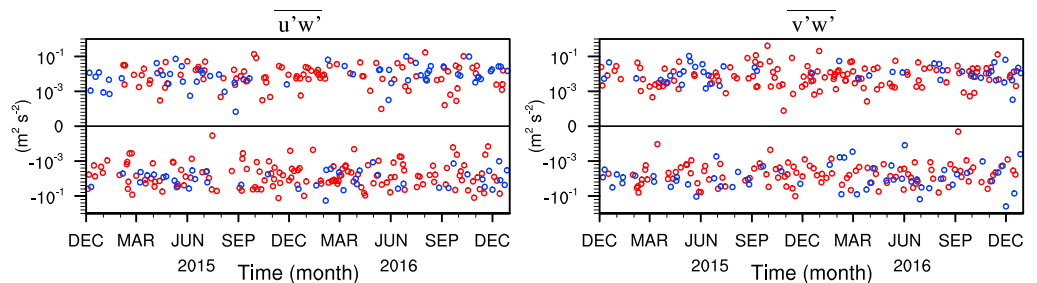


**Figure 14.** Scatter plots of the zonal (left) and meridional (right) momentum fluxes per unit mass averaged in the stratosphere (upper) and troposphere (lower) for each observed wave. The red and blue circles denote upward and downward propagating waves, respectively.

have more negative  $\overline{u'w'}$  than positive values with comparable number of both positive and negative  $\overline{v'w'}$ . The magnitude of the zonal MF by up-going IGWs varies within a range from  $10^{-4}$  to  $10^{-2}$   $\text{m}^2/\text{s}^2$ , with some extremely greater negative magnitudes extending to  $10^{-1}$   $\text{m}^2/\text{s}^2$ , while that by down-going IGWs is greater than  $10^{-2}$   $\text{m}^2/\text{s}^2$  and reaches up to  $10^{-1}$   $\text{m}^2/\text{s}^2$ . The magnitude of the meridional MFs is similar to that of the zonal MFs. Zonal and meridional MFs averaged in the troposphere are  $-0.0018$  and  $0.001$   $\text{m}^2/\text{s}^2$ , respectively, and both up-going and down-going waves do not have directional preferences for the MFs. The tropospheric MFs of both up-going and down-going IGWs have larger values than those in the stratosphere due to the fact that the intrinsic frequency is approximately double, and the Brunt-Väisälä frequency is approximately half in the troposphere regardless of the relatively small amplitudes in the wind perturbations.

#### 4. Discussion

A comprehensive analysis of IGWs is conducted for the first time using radiosonde observation data at JBS, which is located between West and East Antarctica. Hence, it is worth comparing the characteristics of IGWs obtained in this study with those from other studies using radiosonde observations at different stations in Antarctica, although each study used a different method for the GW analysis at different altitudes.

##### 4.1. Propagation of IGWs

A significant enhancement in down-going IGWs in the winter stratosphere has been identified in many studies. Moffat-Griffin et al. (2011) reported that the proportion of down-going GWs exceeds (approximately 60% of the total number of waves) that of up-going GWs in the altitudinal region of 15–22 km at Rothera Station in the winter months (June to August). Similarly, Murphy et al. (2014) noted that the increase in down-going waves (40–60% of the total number of waves) coincides with the reduction in the number of up-going cases in the winter stratosphere in the 15- to 31-km altitude region from May to October. Due to the lack of balloons that reach  $z = 22$  km in the present study, especially for winter months, a direct

comparison between the current study and previous studies is not straightforward. Nevertheless, the strong seasonal variations in the number of up-going and down-going waves (shown in Figure 8) agree well with the previous results.

The dominant westward intrinsic phase velocity of the up-going IGWs observed in the stratosphere (Figure 10) is consistent with Yoshiki et al. (2004), who showed a high probability density of westward propagating GWs relative to the mean wind observed in an altitudinal region of 15–25 km from autumn to spring at Syowa Station. Moffat-Griffin and Colwell (2017) also noted that the up-going waves observed at Halley Station propagate predominantly westward between March and November in the stratosphere (15–22 km). The prominent westward propagation of the down-going IGWs in this study is also consistent with the high-frequency westward propagating down-going waves at Halley (Moffat-Griffin & Colwell, 2017) and Rothera (Moffat-Griffin et al., 2011) Stations.

#### 4.2. Intrinsic Frequency and Wavelengths

The characteristics of the observed GWs highly depend on the measurement techniques, which have their own limitations based on the observational filter (Alexander, 1998), and the analysis method applied to the measured data. Particularly, high-resolution radiosonde data, such as those used in the present study, enable us to detect GWs with short vertical wavelength components. In this study, the dominant vertical wavelength of IGWs is approximately 1–2 km in both the troposphere and the stratosphere; this is comparable to the monthly mean vertical wavelength of 1.5 km reported by Innis et al. (2004) in the altitudinal region of 12–20 km from three radiosonde stations in East Antarctica (Casey, Davis, and Mawson Stations).

It is worth noting that the maximum resolvable vertical wavelength in the troposphere and stratosphere largely depends on the depth of each analysis layer, and the constraints of the depth may lead to relatively weak power for long vertical wavelength components if the depth is too shallow. The depth of the analysis layer in the present study (5-km depth in the troposphere and 7-km depth in the stratosphere) is somewhat shallow, which is determined to apply the same analysis layer to all months to safely avoid the impacts of the tropopause, although there are strong monthly variations in the tropopause height at JBS (Figure 6). An additional calculation of the vertical wavelength in the troposphere during October 2015 with a deeper analysis layer (8-km depth between 2 and 10 km) demonstrates that the monthly mean value of the vertical wavelength is somewhat longer (1.9 km) than that (1.4 km) in the original analysis (not shown). The increase in vertical wavelength from this additional calculation results in a slight increase in the horizontal wavelength from 67.7 to 68.9 km via the dispersion relationship of IGWs (equation (15)).

Murphy et al. (2014) found that waves with a vertical wavelength less than 2–3 km (median value of 1 km) are dominant in the altitudinal region of 15–31 km at Davis Station using the wavelet analysis method. Although the depth of analysis layer (16 km) in Murphy et al. (2014) is quite deeper than that (7 km) in this study, the dominant vertical wavelengths are similar to those observed in this study due to the use of Morlet wavelet. Moffat-Griffin and Colwell (2017) also noted that the waves with vertical wavelengths less than 2 km are dominant at Halley Station in the altitudinal region of 15–22 km as the wavelet analysis technique is applied. Meanwhile, the vertical wavelengths of GWs reported by Yoshiki and Sato (2000) and Yoshiki et al. (2004) at Syowa Station are quite longer (approximately 3–4 km) than those obtained from the current study and the aforementioned studies at other radiosonde stations in Antarctica. This is likely due to the fact that Yoshiki and Sato (2000) and Yoshiki et al. (2004) applied a particular band-pass filter (2–8 km) to the vertical profiles of the perturbations; therefore, GWs with vertical wavelengths less than 2 km were artificially reduced.

#### 4.3. Wave Energy

In previous studies on the climatology of GWs, some common features in GW energies have been found: The kinetic energy reaches a maximum in winter above a height of 25 km, while the potential energy reaches a maximum in spring at an altitudinal range of 15–26 km (Murphy et al., 2014; Pfenninger et al., 1999; Yoshiki et al., 2004; Yoshiki & Sato, 2000). Meanwhile, Moffat-Griffin et al. (2011) identified two peaks in the wave energy at the spring and autumn equinoxes, which is related to the seasonal variation in the critical-level filtering of orographically induced GWs over the Antarctic Peninsula and down-going waves generated from the stratospheric polar vortex. This feature has not been observed in the aforementioned studies at Davis,

Amundsen-Scott, and Syowa Stations, which are located far from significant topographies. The annual variations in the wave energies observed in this study are more similar to those in Moffat-Griffin et al. (2011). Sources that contribute to the seasonal variations in wave energy that are observed in this study will be precisely examined in Part 2 by taking into account the extreme mountains located on the windward side of JBS as well as the polar night jet and tropospheric disturbances approaching the station (Yoshiki et al., 2004).

The monthly averages of kinetic (2.5–6.0 J/kg) and potential (0.5–1.7 J/kg) energies in the stratosphere are comparable to those from some previous studies, such as Pfenninger et al. (1999) over the South Pole (Amundsen-Scott Station; 1–11 and 0.5–3 J/kg, respectively) and Yoshiki et al. (2004) at Syowa Station (2–5 and 0.5–4 J/kg, respectively) at an altitudinal region of 15–25 km. On the other hand, the kinetic (potential) energies at Rothera Station reported by Moffat-Griffin et al. (2011; 0.2–0.7 [0.2–0.5] J/kg) and Davis Station reported by Murphy et al. (2014; 0.3–0.8 [0.1–0.3] J/kg) are much smaller than those of the current study at JBS and the aforementioned Syowa Station and South Pole. The magnitude of the wave energy is highly dependent on the methods used for the GWs analysis, including the techniques for extracting the perturbations, the depth and height of the analysis layer, and the statistical method for averaging. Murphy et al. (2014) noted that the wavelet technique used for extracting wave perturbations tends to decrease wave energies and the use of log-normal averaging can reduce the averaged wave energies by decreasing extremely large values in the kinetic and potential energy cases.

The monthly averaged ratio of kinetic energy to potential energy ( $E_K/E_P$ ) in the stratosphere ranges from 2.5 to 6.5 in the present study, and it is comparable to that of 2–9 in Pfenninger et al. (1999), 1–4 in Yoshiki et al. (2004), and 2.5–4 in Murphy et al. (2014) but larger than that of 0.5–1.5 in Moffat-Griffin et al. (2011), of which the altitudinal region (15–22 km) considered is the same as in the current study. Based on the linear theory of GWs,  $E_K/E_P$  should be between 5/3 and 2 for steady and freely propagating GWs (Fritts & Vanzandt, 1993). The observed ratio in the stratosphere in the current study is much greater than the theoretical value, suggesting that the waves are not in a state of free propagation and are far from the source. According to Huang et al. (2002), a GW that is newly excited by a momentum (thermal) source could have a large  $E_K$  ( $E_P$ ) based on numerical simulations, implying that the observed IGWs in the current study in the stratosphere may be excited by momentum sources. This possibility will be examined in Part 2, where the sources of the observed GWs at JBS will be investigated.

#### 4.4. GW Momentum Flux

Sato and Yoshiki (2008) reported that up-going GWs mostly have negative zonal MFs in March, June, and October, while down-going GWs in June primarily have positive zonal MFs based on radiosonde observation at Syowa Station. This is similar to the current result shown in Figure 14a, which shows the more negative (positive) sign of zonal MFs of up-going (down-going) IGWs in the stratosphere, although several up-going IGWs have positive zonal MF. This indicates that many stratospheric IGWs propagate westward relative to the westerly background wind, especially in the period during autumn to spring. This is also true in December as well, which is different from the result reported by Sato and Yoshiki (2008) with the dominant eastward MF observed in December. Regarding the meridional MF, dominant positive MFs in down-going IGWs in the stratosphere (Figure 14a) are consistent with the results in Sato and Yoshiki (2008), but the preferred negative MF in up-going IGWs in winter and spring, which is shown in Sato and Yoshiki (2008), is not observed in this study.

The zonal and meridional MFs in Sato and Yoshiki (2008) range from  $-0.1$  to  $0.04$   $\text{m}^2/\text{s}^2$  and  $-0.2$  to  $0.06$   $\text{m}^2/\text{s}^2$ , respectively. Although a direct comparison in the magnitude between Sato and Yoshiki (2008) and the current study is not straightforward, due to different methodologies applied and different analysis periods considered, the magnitudes of MFs are quite similar to each other. Furthermore, much larger values of zonal and meridional MFs in March and October compared to those in December shown in Sato and Yoshiki (2008) are consistent with the large zonal and meridional MFs in autumn and spring (greater than  $0.1$   $\text{m}^2/\text{s}^2$ ) in Figure 14a of this study. The average zonal ( $0.0016$   $\text{m}^2/\text{s}^2$  in summer and  $0.0044$   $\text{m}^2/\text{s}^2$  in winter) and meridional MFs ( $-0.00014$   $\text{m}^2/\text{s}^2$  in summer and  $0.0011$   $\text{m}^2/\text{s}^2$  in winter) at Davis Station shown in Murphy et al. (2014) are also in the same order of magnitude of the current study (zonal MF:  $-0.0063$   $\text{m}^2/\text{s}^2$  in summer and  $-0.011$   $\text{m}^2/\text{s}^2$  in winter; meridional MF:  $-0.0019$   $\text{m}^2/\text{s}^2$  in summer and  $0.0026$   $\text{m}^2/\text{s}^2$  in winter).

## 5. Summary and Conclusions

In this study, operational radiosonde data collected at JBS (74°37'S, 164°13'E) for 25 months from December 2014 to December 2016 are analyzed to investigate the characteristics of IGWs.

Given that this is the first year-round radiosonde observation conducted at a new Antarctic station JBS at high latitude, we examined wind and temperature revealed in the radiosonde data, prior to investigating the characteristics of IGWs. In the lower troposphere, strong katabatic winds appear without a directional preference and without seasonal variations. In the stratosphere above  $z = 15$  km, the zonal wind is dominated by westerlies, except for summer (DJF), with the maximum speed of 122 m/s in the polar night jet. The meridional wind has stronger temporal variations than the zonal wind, with a typical speed ranging from  $-40$  to 50 m/s without height dependency. During the permanent dark from May to September, an extremely cold and stable atmosphere is formed near the surface as well as in the lower stratosphere; the temperature in the lower stratosphere dropped to a minimum of 179 K at an altitudinal region of 15–25 km. As the polar vortex is being weakened in September, warming occurs above the midstratosphere and propagate to the lower stratosphere, resulting in high static stability with a strong vertical temperature gradient. To assess the ability of the global reanalyses to represent wind and temperature over JBS, a comparison between four global reanalysis (CFSv2, MERRA, ERA-Interim, and NCEP/DOE R2) data sets and our radiosonde observations is conducted. In the troposphere, reanalyses with a coarse horizontal resolution have significant negative (positive) biases in the zonal (meridional) wind, suggesting that winds over the complex topography at JBS, which is surrounded by the steep Transantarctic Mountains and the coastal line of the Ross Sea, are not represented well in the models. In the stratosphere, remarkable underestimations of the polar night jet and cold (warm) biases in early spring (winter) appear in all reanalyses.

Based on the quasi-monochromatic wave theory (Vincent et al., 1997), the Stokes parameter spectra method and the rotary spectrum method are applied to examine the characteristics of IGWs in the troposphere ( $z = 2$ –7 km) and lower stratosphere ( $z = 15$ –22 km). The characteristics, energies, and MFs of IGWs obtained from the current study are summarized as follows.

The vertical propagation direction of IGWs has clear seasonal variations in the stratosphere. The number of down-going IGWs increases from late autumn to early spring, whereas up-going IGWs appear more often than down-going IGWs. Significant flow imbalance represented by large  $RNBE$  is observed in the upper stratosphere during the period when down-going IGWs appear in the stratospheric analysis layer, implying the polar night jet in the upper stratosphere to be a source of the observed IGWs. In the troposphere, approximately 60% (40%) of IGWs propagate upward (downward) without a seasonal preference. Hence, it can be inferred that some waves could be generated from sources in the layer between the upper troposphere and the lower stratosphere.

Both up-going and down-going IGWs in the stratosphere prevalently direct westward relative to the background wind, with a speed less than 10 m/s, whereas both up-going and down-going IGWs have isotropic directional distributions in the troposphere. Due to the strong background wind, most of IGWs tend to be advected to the east.

In the troposphere (stratosphere), the mean values of intrinsic frequency, vertical wavelength, and horizontal wavelength for IGWs observed at JBS are 3.57f (1.93f), 1.48 (1.48) km, and 63.06 (221.81) km, respectively. There are clear differences in the intrinsic frequency and horizontal wavelength between the two analysis layers, whereas the vertical wavelengths seem to be similar.

The total wave energy of IGWs has a much greater value in the stratosphere, with some large values in autumn (MAM) and spring (SON), while that in the troposphere has a much smaller value without seasonal preference. The ratio of kinetic energy to potential energy ( $E_k/E_p$ ) in the stratosphere has a range from 2.5 to 6.5, which is greater than the theoretical value (from 5/3 to 2) but similar to those reported in previous studies at other Antarctic stations.

The zonal and meridional MFs averaged in the stratosphere (troposphere) are  $-0.008$  ( $-0.0018$ ) and  $-0.0005$  ( $0.001$ )  $m^2/s^2$ , respectively. In the stratosphere, up-going IGWs have more westward and both northward and southward MFs, while most of down-going IGWs have eastward and northward MFs. In the troposphere, remarkable directional preferences for the zonal and meridional MFs are not observed, and the individual values are larger than the MFs in the stratosphere.



In Part 2, the sources of the observed IGWs at JBS will be investigated in detail using a three-dimensional ray-tracing model.

### Acknowledgments

The authors thank two anonymous reviewers for their careful reading of the manuscript and helpful comments. This study was conducted while the third author (H. Y. C.) was in her sabbatical leave. This work was supported by research fund PE18020 from Korea Polar Research Institute. The authors appreciate the support of the Korea Polar Research Institute for the radiosonde data. The authors would also like to thank for providing access to the reanalysis data sets ERA-Interim (<http://apps.ecmwf.int/datasets/data/>), CFSv2 (<http://rda.ucar.edu>), MERRA and MERRA2 (<https://goldsmr5.gesdisc.eosdis.nasa.gov/>), and NCEP/DOE R2 (<http://www.cdc.noaa.gov/>). Further thanks to the Antarctic Meteorological Observatory of the Programma Nazionale di Ricerche in Antartide for the provision of radiosonde data from Mario Zucchelli Station (<http://www.climantaride.it>).

### References

- Alexander, M. J. (1998). Interpretations of observed climatological patterns in stratospheric gravity wave variance. *Journal of Geophysical Research*, 103(D8), 8627–8640. <https://doi.org/10.1029/97JD03325>
- Alexander, M. J., Geller, M., McLandress, C., Polavarapu, S., Preusse, P., Sassi, F., et al. (2010). Recent developments in gravity-wave effects in climate models and the global distribution of gravity-wave momentum flux from observations and models. *Quarterly Journal of the Royal Meteorological Society*, 136(650), 1103–1124. <https://doi.org/10.1002/qj.637>
- Alexander, S. P., Orr, A., Webster, S., & Murphy, D. J. (2017). Observations and fine-scale model simulations of gravity waves over Davis, East Antarctica (69° S, 78° E). *Journal of Geophysical Research: Atmospheres*, 122, 7355–7370. <https://doi.org/10.1002/2017JD026615>
- Andrews, D. G., Holton, J. R., & Leovy, C. B. (1987). *Middle atmosphere dynamics* (no. 40). New York: Academic press.
- Bracegirdle, T. J., & Marshall, G. J. (2012). The reliability of Antarctic tropospheric pressure and temperature in the latest global reanalyses. *Journal of Climate*, 25(20), 7138–7146. <https://doi.org/10.1175/JCLI-D-11-00685.1>
- Butchart, N., Cionni, I., Eyring, V., Shepherd, T. G., Waugh, D. W., Akiyoshi, H., et al. (2010). Chemistry–climate model simulations of twenty-first century stratospheric climate and circulation changes. *Journal of Climate*, 23(20), 5349–5374. <https://doi.org/10.1175/2010JCLI3404.1>
- Choi, H.-J., & Chun, H.-Y. (2013). Effects of convective gravity wave drag in the Southern Hemisphere winter stratosphere. *Journal of the Atmospheric Sciences*, 70(7), 2120–2136. <https://doi.org/10.1175/JAS-D-12-0238.1>
- Chun, H.-Y., Goh, J.-S., & Kim, Y.-H. (2007). Characteristics of inertio-gravity waves revealed in rawinsonde data observed in Korea during 20 August to 5 September 2002. *Journal of Geophysical Research*, 112, D16108. <https://doi.org/10.1029/2006JD008348>
- Chun, H.-Y., Kim, Y.-H., Choi, H.-J., & Kim, J.-Y. (2011). Influence of gravity waves in the tropical upwelling: WACCM simulations. *Journal of the Atmospheric Sciences*, 68(11), 2599–2612. <https://doi.org/10.1175/JAS-D-11-022.1>
- Chun, H.-Y., Shin, S.-W., & Kim, Y.-H. (2014). Spatiotemporal variations in the diagnostics of gravity waves associated with jet/front system and their correlations with GWs revealed in high-resolution global reanalysis data, Paper presented at EGU General Assembly 2014, Vienna, Austria.
- Dee, D. P., Uppala, S. M., Simmons, A. J., Berrisford, P., Poli, P., Kobayashi, S., et al. (2011). The ERA-Interim reanalysis: Configuration and performance of the data assimilation system. *Quarterly Journal of the Royal Meteorological Society*, 137(656), 553–597. <https://doi.org/10.1002/qj.828>
- Eckermann, S. D. (1996). Hodographic analysis of gravity waves: Relationships among Stokes parameters, rotary spectra and cross-spectral methods. *Journal of Geophysical Research*, 101(D14), 19,169–19,174. <https://doi.org/10.1029/96JD01578>
- Eckermann, S. D., & Vincent, R. A. (1989). Falling sphere observations of anisotropic gravity wave motions in the upper stratosphere over Australia. *Pure and Applied Geophysics*, 130(2–3), 509–532. <https://doi.org/10.1007/BF00874472>
- Elvidge, A. D., Renfrew, I. A., King, J. C., Orr, A., & Lachlan-Cope, T. A. (2016). Foehn warming distributions in nonlinear and linear flow regimes: A focus on the Antarctic Peninsula. *Quarterly Journal of the Royal Meteorological Society*, 142(695), 618–631. <https://doi.org/10.1002/qj.2489>
- Ern, M., Preusse, P., Alexander, M. J., & Warner, C. D. (2004). Absolute values of gravity wave momentum flux derived from satellite data. *Journal of Geophysical Research*, 109, D20103. <https://doi.org/10.1029/2004JD004752>
- Feng, S., Fu, Y., & Xiao, Q. (2012). Trends in the global tropopause thickness revealed by radiosondes. *Geophysical Research Letters*, 39, L20706. <https://doi.org/10.1029/2012GL053460>
- Fritts, D. C., & Alexander, M. J. (2003). Gravity wave dynamics and effects in the middle atmosphere. *Reviews of Geophysics*, 41(1), 1003. <https://doi.org/10.1029/2001RG000106>
- Fritts, D. C., Janches, D., Iimura, H., Hocking, W. K., Bageston, J. V., & Leme, N. M. P. (2012). Drake Antarctic Agile Meteor Radar first results: Configuration and comparison of mean and tidal wind and gravity wave momentum flux measurements with Southern Argentina Agile Meteor Radar. *Journal of Geophysical Research*, 117, D02105. <https://doi.org/10.1029/2011JD016651>
- Fritts, D. C., & Vanzandt, T. E. (1993). Spectral estimates of gravity wave energy and momentum fluxes. Part I: Energy dissipation, acceleration, and constraints. *Journal of the Atmospheric Sciences*, 50(22), 3685–3694. [https://doi.org/10.1175/1520-0469\(1993\)050<3685:SEOGWE>2.0.CO;2](https://doi.org/10.1175/1520-0469(1993)050<3685:SEOGWE>2.0.CO;2)
- García, R. R., & Boville, B. A. (1994). “Downward control” of the mean meridional circulation and temperature distribution of the polar winter stratosphere. *Journal of the Atmospheric Sciences*, 51(15), 2238–2245. [https://doi.org/10.1175/1520-0469\(1994\)051<2238:COTMMC>2.0.CO;2](https://doi.org/10.1175/1520-0469(1994)051<2238:COTMMC>2.0.CO;2)
- García, R. R., Smith, A. K., Kinnison, D. E., Cámara, Á. D. L., & Murphy, D. J. (2017). Modification of the gravity wave parameterization in the Whole Atmosphere Community Climate Model: Motivation and results. *Journal of the Atmospheric Sciences*, 74(1), 275–291. <https://doi.org/10.1175/JAS-D-16-0104.1>
- Gelaro, R., McCarty, W., Suárez, M. J., Todling, R., Molod, A., Takacs, L., et al. (2017). The modern-era retrospective analysis for research and applications, version 2 (MERRA-2). *Journal of Climate*, 30(14), 5419–5454. <https://doi.org/10.1175/JCLI-D-16-0758.1>
- Geller, M. A., Alexander, M. J., Love, P. T., Bacmeister, J., Ern, M., Hertzog, A., et al. (2013). A comparison between gravity wave momentum fluxes in observations and climate models. *Journal of Climate*, 26(17), 6383–6405. <https://doi.org/10.1175/JCLI-D-12-00545.1>
- Hertzog, A., Boccara, G., Vincent, R. A., Vial, F., & Cocquerez, P. (2008). Estimation of gravity wave momentum flux and phase speeds from quasi-Lagrangian stratospheric balloon flights. Part II: Results from the Vorcore campaign in Antarctica. *Journal of the Atmospheric Sciences*, 65(10), 3056–3070. <https://doi.org/10.1175/2008JAS2710.1>
- Hertzog, A., Cocquerez, P., Guilbon, R., Valdivia, J. N., Venel, S., Basdevant, C., et al. (2007). Stratéole/Vorcore—Long-duration, superpressure balloons to study the Antarctic lower stratosphere during the 2005 winter. *Journal of Atmospheric and Oceanic Technology*, 24(12), 2048–2061. <https://doi.org/10.1175/2007JTECHA948.1>
- Hines, C. Q. (1989). Tropopausal mountain waves over Arecibo: A case study. *Journal of the Atmospheric Sciences*, 46(4), 476–488. [https://doi.org/10.1175/1520-0469\(1989\)046<0476:TMWOAA>2.0.CO;2](https://doi.org/10.1175/1520-0469(1989)046<0476:TMWOAA>2.0.CO;2)
- Huang, C. M., Zhang, S. D., & Yi, F. (2002). A numerical study of the nonlinear propagation of gravity-wave packets excited by temperature disturbance. *Chinese Journal of Space Science*, 22, 330–338.
- Innis, J. L., Klekociuk, A. R., Morris, R. J., Cunningham, A. P., Graham, A. D., & Murphy, D. J. (2008). A study of the relationship between stratospheric gravity waves and polar mesospheric clouds at Davis Antarctica. *Journal of Geophysical Research*, 113, D14102. <https://doi.org/10.1029/2007JD009031>

- Innis, J. L., Klekociuk, A. R., & Vincent, R. A. (2004). Interstation correlation of high-latitude lower-stratosphere gravity wave activity: Evidence for planetary wave modulation of gravity waves over Antarctica. *Journal of Geophysical Research*, *109*, D17106. <https://doi.org/10.1029/2004JD004961>
- Jiang, J. H., Wu, D. L., & Eckermann, S. D. (2002). Upper Atmosphere Research Satellite (UARS) MLS observation of mountain waves over the Andes. *Journal of Geophysical Research*, *107*(D20), 8273. <https://doi.org/10.1029/2002JD002091>
- Kanamitsu, M., Ebisuzaki, W., Woollen, J., Yang, S. K., Hnilo, J. J., Fiorino, M., & Potter, G. L. (2002). NCEP–DOE AMIP-II reanalysis (R-2). *Bulletin of the American Meteorological Society*, *83*(11), 1631–1644. <https://doi.org/10.1175/BAMS-83-11-1631>
- Ki, M.-O., & Chun, H.-Y. (2010). Characteristics and sources of inertia-gravity waves revealed in the KEOP-2007 radiosonde data. *Asia-Pacific Journal of Atmospheric Sciences*, *46*(3), 261–277. <https://doi.org/10.1007/s13143-010-1001-4>
- Ki, M.-O., & Chun, H.-Y. (2011). Inertia gravity waves associated with deep convection observed during the summers of 2005 and 2007 in Korea. *Journal of Geophysical Research*, *116*, D16122. <https://doi.org/10.1029/2011JD015684>
- Kim, Y.-H., & Chun, H.-Y. (2015). Contributions of equatorial wave modes and parameterized gravity waves to the tropical QBO in HadGEM2. *Journal of Geophysical Research: Atmospheres*, *120*, 1065–1090. <https://doi.org/10.1002/2014JD022174>
- Kim, Y.-J., Eckermann, S. D., & Chun, H.-Y. (2003). An overview of the past, present and future of gravity-wave drag parametrization for numerical climate and weather prediction models. *Atmosphere-Ocean*, *41*(1), 65–98. <https://doi.org/10.3137/ao.410105>
- King, J. C. (1990). Some measurements of turbulence over an Antarctic ice shelf. *Quarterly Journal of the Royal Meteorological Society*, *116*(492), 379–400. <https://doi.org/10.1002/qj.49711649208>
- Lalas, D. P., & Einaudi, F. (1980). Tropospheric gravity waves: Their detection by and influence on rawinsonde balloon data. *Quarterly Journal of the Royal Meteorological Society*, *106*(450), 855–864. <https://doi.org/10.1002/qj.49710645014>
- Lindzen, R. S. (1981). Turbulence and stress owing to gravity wave and tidal breakdown. *Journal of Geophysical Research*, *86*(C10), 9707–9714. <https://doi.org/10.1029/JC086iC10p09707>
- Love, P. T., & Murphy, D. J. (2016). Gravity wave momentum flux in the mesosphere measured by VHF radar at Davis, Antarctica. *Journal of Geophysical Research: Atmospheres*, *121*, 12,723–12,736. <https://doi.org/10.1002/2016JD025627>
- Matsuda, T. S., Nakamura, T., Ejiri, M. K., Tsutsumi, M., Tomikawa, Y., Taylor, M. J., et al. (2017). Characteristics of mesospheric gravity waves over Antarctica observed by Antarctic Gravity Wave Instrument Network imagers using 3-D spectral analyses. *Journal of Geophysical Research: Atmospheres*, *122*, 8969–8981. <https://doi.org/10.1002/2016JD026217>
- McLandress, C., Shepherd, T. G., Polavarapu, S., & Beagley, S. R. (2012). Is missing orographic gravity wave drag near 60°S the cause of the stratospheric zonal wind biases in chemistry–climate models? *Journal of the Atmospheric Sciences*, *69*(3), 802–818. <https://doi.org/10.1175/JAS-D-11-0159.1>
- Moffat-Griffin, T., & Colwell, S. R. (2017). The characteristics of the lower stratospheric gravity wavefield above Halley (75°S, 26°W), Antarctica, from radiosonde observations. *Journal of Geophysical Research: Atmospheres*, *122*, 8998–9010. <https://doi.org/10.1002/2017JD027079>
- Moffat-Griffin, T., Hibbins, R. E., Jarvis, M. J., & Colwell, S. R. (2011). Seasonal variations of gravity wave activity in the lower stratosphere over an Antarctic Peninsula station. *Journal of Geophysical Research*, *116*, D14111. <https://doi.org/10.1029/2010JD015349>
- Murphy, D. J., Alexander, S. P., Klekociuk, A. R., Love, P. T., & Vincent, R. A. (2014). Radiosonde observations of gravity waves in the lower stratosphere over Davis, Antarctica. *Journal of Geophysical Research: Atmospheres*, *119*, 11,973–11,996. <https://doi.org/10.1002/2014JD022448>
- Pfenninger, M., Liu, A. Z., Papen, G. C., & Gardner, C. S. (1999). Gravity wave characteristics in the lower atmosphere at South Pole. *Journal of Geophysical Research*, *104*(D6), 5963–5984. <https://doi.org/10.1029/98JD02705>
- Plougonven, R., & Zhang, F. (2016). Gravity waves generated by jets and fronts and their relevance for clear-air turbulence. In *Aviation Turbulence* (pp. 385–406). Cham: Springer.
- Preusse, P., Ern, M., Bechtold, P., Eckermann, S. D., Kalisch, S., Trinh, Q. T., & Riese, M. (2014). Characteristics of gravity waves resolved by ECMWF. *Atmospheric Chemistry and Physics*, *14*(19), 10,483–10,508. <https://doi.org/10.5194/acp-14-10483-2014>
- Randel, W. J., Garcia, R., & Wu, F. (2008). Dynamical balances and tropical stratospheric upwelling. *Journal of the Atmospheric Sciences*, *65*(11), 3584–3595. <https://doi.org/10.1175/2008JAS2756.1>
- Rienecker, M. M., Suarez, M. J., Gelaro, R., Todling, R., Bacmeister, J., Liu, E., et al. (2011). MERRA: NASA’s modern-era retrospective analysis for research and applications. *Journal of Climate*, *24*(14), 3624–3648. <https://doi.org/10.1175/JCLI-D-11-00015.1>
- Rourke, S., Mulligan, F. J., French, W. J. R., & Murphy, D. J. (2017). A climatological study of short-period gravity waves and ripples at Davis Station, Antarctica (68°S, 78°E), during the (austral winter February–October) period 1999–2013. *Journal of Geophysical Research: Atmospheres*, *122*, 11,388–11,404. <https://doi.org/10.1002/2017JD026998>
- Saha, S., Moorthi, S., Pan, H. L., Wu, X., Wang, J., Nadiga, S., et al. (2010). The NCEP climate forecast system reanalysis. *Bulletin of the American Meteorological Society*, *91*(8), 1015–1058. <https://doi.org/10.1175/2010BAMS3001.1>
- Saha, S., Moorthi, S., Wu, X., Wang, J., Nadiga, S., Tripp, P., et al. (2014). The NCEP climate forecast system version 2. *Journal of Climate*, *27*(6), 2185–2208. <https://doi.org/10.1175/JCLI-D-12-00823.1>
- Sato, K., Watanabe, S., Kawatani, Y., Tomikawa, Y., Miyazaki, K., & Takahashi, M. (2009). On the origins of mesospheric gravity waves. *Geophysical Research Letters*, *36*, L19801. <https://doi.org/10.1029/2009GL039908>
- Sato, K., & Yoshiki, M. (2008). Gravity wave generation around the polar vortex in the stratosphere revealed by 3-hourly radiosonde observations at Syowa Station. *Journal of the Atmospheric Sciences*, *65*(12), 3719–3735. <https://doi.org/10.1029/2008JAS2539.1>
- Vincent, R. A. (1984). Gravity-wave motions in the mesosphere. *Journal of Atmospheric and Terrestrial Physics*, *46*(2), 119–128. [https://doi.org/10.1016/0021-9169\(84\)90137-5](https://doi.org/10.1016/0021-9169(84)90137-5)
- Vincent, R. A., & Alexander, M. J. (2000). Gravity waves in the tropical lower stratosphere: An observational study of seasonal and interannual variability. *Journal of Geophysical Research*, *105*(D14), 17,971–17,982. <https://doi.org/10.1029/2000JD900196>
- Vincent, R. A., Allen, S. J., & Eckermann, S. D. (1997). Gravity-wave parameters in the lower stratosphere. In *Gravity wave processes* (pp. 7–25). Berlin, Heidelberg: Springer. [https://doi.org/10.1007/978-3-642-60654-0\\_2](https://doi.org/10.1007/978-3-642-60654-0_2)
- Wang, J.-W., Kim, J.-J., Choi, W., Mun, D.-S., Kang, J.-E., Kwon, H., et al. (2017). Effects of wind fences on the wind environment around Jang Bogo Antarctic Research Station. *Advances in Atmospheric Sciences*, *34*(12), 1404–1414. <https://doi.org/10.1007/s00376-017-6333-x>
- Wang, L., Geller, M. A., & Alexander, M. J. (2005). Spatial and temporal variations of gravity wave parameters. Part I: Intrinsic frequency, wavelength, and vertical propagation direction. *Journal of the Atmospheric Sciences*, *62*(1), 125–142. <https://doi.org/10.1175/JAS-3364.1>
- World Meteorological Organization (1957). A three-dimensional science: Second session of the commission for aerology. *WMO Bulletin*, *4*(2), 134–138.
- Wu, D. L., & Jiang, J. H. (2002). MLS observations of atmospheric gravity waves over Antarctica. *Journal of Geophysical Research*, *107*(D24), 4773. <https://doi.org/10.1029/2002JD002390>

- Yamashita, C., Chu, X., Liu, H. L., Espy, P. J., Nott, G. J., & Huang, W. (2009). Stratospheric gravity wave characteristics and seasonal variations observed by lidar at the South Pole and Rothera, Antarctica. *Journal of Geophysical Research*, *114*, D12101. <https://doi.org/10.1029/2008JD011472>
- Yoshiki, M., Kizu, N., & Sato, K. (2004). Energy enhancements of gravity waves in the Antarctic lower stratosphere associated with variations in the polar vortex and tropospheric disturbances. *Journal of Geophysical Research*, *109*, D23104. <https://doi.org/10.1029/2004JD004870>
- Yoshiki, M., & Sato, K. (2000). A statistical study of gravity waves in the polar regions based on operational radiosonde data. *Journal of Geophysical Research*, *105*(D14), 17,995–18,011. <https://doi.org/10.1029/2000JD900204>
- Zängl, G., & Hoinka, K. P. (2001). The tropopause in the polar regions. *Journal of Climate*, *14*(14), 3117–3139. [https://doi.org/10.1175/1520-0442\(2001\)014<3117:TTITPR>2.0.CO;2](https://doi.org/10.1175/1520-0442(2001)014<3117:TTITPR>2.0.CO;2)
- Zhang, F. (2004). Generation of mesoscale gravity waves in upper-tropospheric jet-front systems. *Journal of the Atmospheric Sciences*, *61*(4), 440–457. [https://doi.org/10.1175/1520-0469\(2004\)061<0440:GOMGWI>2.0.CO;2](https://doi.org/10.1175/1520-0469(2004)061<0440:GOMGWI>2.0.CO;2)